



Remarkable activity and stability of Ni catalyst supported on CeO₂-Al₂O₃ via CeAlO₃ perovskite towards glycerol steam reforming for hydrogen production

Krongthong Kamonsuangkasem^a, Supaporn Therdthianwong^{b,*},
Apichai Therdthianwong^c, Nirawat Thammajak^d

^a Joint Graduate School of Energy and Environment, King Mongkut's University of Technology Thonburi, 126 Pracha Uthit Rd., Bang Mod, Thung Khru, Bangkok, 10140, Thailand

^b Department of Chemical Engineering, Faculty of Engineering, King Mongkut's University of Technology Thonburi, 126 Pracha Uthit Rd., Bang Mod, Thung Khru, Bangkok, 10140, Thailand

^c Fuel Cells and Hydrogen Research and Engineering Center, Clean Energy System Group, Pilot Plant Development and Training Institute, King Mongkut's University of Technology Thonburi, 126 Pracha Uthit Rd., Bang Mod, Thung Khru, Bangkok, 10140, Thailand

^d Synchrotron Light Research Institute (Public Organization), 111 University Avenue, Muang District, Nakhon Ratchasima, 30000, Thailand

ARTICLE INFO

Article history:

Received 28 February 2017

Received in revised form 9 June 2017

Accepted 23 June 2017

Available online 24 June 2017

Keywords:

Glycerol steam reforming (GSR)

Hydrogen production

CeO₂-Al₂O₃

CeAlO₃ perovskite

Coking inhibition

ABSTRACT

The effects of CeO₂-Al₂O₃ mixed oxide preparation methods on the physical and chemical properties of CeO₂-Al₂O₃, and the catalytic performance toward glycerol steam reforming (GSR) over the CeO₂-Al₂O₃-supported Ni catalysts were investigated. Three CeO₂-Al₂O₃ supports were prepared by a single-step sol-gel (SS) of ceria and alumina precursors, followed by the impregnations of ceria precursors on both a xerogel Al₂O₃ (IS) and a commercial Al₂O₃ (IC). The characterization techniques used were N₂ adsorption-desorption, H₂-chemisorption, XRD, H₂-TPR, NH₃-TPD, XANES, XPS and TGA. The sol-gel derived supports generate not only a well-developed mesoporous structure, but also the incorporation of the Ce species into the Al₂O₃ structure forming CeAlO₃ perovskite. This formation suppresses the interaction between Ni and Al₂O₃, thereby increasing the number of active and Brønsted acid sites to improve the bifunctional metal-acid properties of Ni/CeO₂-Al₂O₃ in the hydrogenolysis and dehydrogenation-dehydration of condensable intermediates that produce more H₂. The formation of CeAlO₃ is remarkably promoted by the single-step sol-gel preparation method, and the catalyst supported on the SS-derived oxide exhibits excellent activity and strong resistances to coke formation, phase transformation, and nickel sintering.

© 2017 Elsevier B.V. All rights reserved.

1. Introduction

As global energy consumption drastically increased during the last half-century, the development of economical and environmentally-friendly renewable energy has been a major challenge. There is no single solution to all energy-related problems, but in recent years, biodiesel has become an alternative energy source for mitigating the energy shortage. A transesterification process, the most common process for biodiesel production, produces about 10 wt% of glycerol as a by-product. Hence, as the production of biodiesel increases, it becomes very important to find a means to utilize such excess glycerol. One alternative that seems promising is the use of glycerol as a renewable source for producing hydrogen.

Steam reforming (SR) is a commercially efficient process for producing hydrogen from fossil fuels, hydrocarbons, alcohols, biomass, etc. The catalytic steam reforming of glycerol has been attracting a great deal of interest, as one mole of glycerol contains four moles of H₂, which is higher amount than that of methanol and ethanol, although the H₂:C mole ratio of glycerol is lower than that of methanol and ethanol. The steam reforming of glycerol involves the rupturing of C–C, O–H, and C–H bonds, except for the C–O ones [1–3] whilst the type of catalyst that is used strongly influences the product yield and selectivity. Much of the research on the catalyst has emphasized noble metals, such as Pt, Pd, Ir, Rh, and Ru [4–12], and non-noble metals, such as Ni [1,13–19], which are supported over several metal oxides, such as Al₂O₃, TiO₂, CeO₂, ZrO₂, SiO₂, and MgO. Among these catalysts, Ni-based catalysts on Al₂O₃ supports have received the most attention due to the catalysts' low cost, availability and ability to break C–C, C–H, and O–H bonds [1,13–15,20]. This type of catalyst also promotes a com-

* Corresponding author. Tel.: 662-470 9222 ext 403; fax: 662-470 9325.

E-mail address: supaporn.the@kmutt.ac.th (S. Therdthianwong).

bined water-gas shift reaction that helps to remove the adsorbed CO from the catalyst's surface [1,15,20]. However, it has been reported that most Ni catalysts suffer severely from coking and metal sintering, which result in the reduction of the catalyst's activity and stability. These deactivations could be lowered by the addition of a promoter, largely in the form of metal oxides, especially lanthanide oxides, onto the Al_2O_3 supports.

CeO_2 , a lanthanide oxide known as an oxygen storage material, has been the most frequently employed as the promoter for $\text{Ni}/\text{Al}_2\text{O}_3$ in several reactions particularly the steam reforming of hydrocarbons and oxygenated compounds [12,15,21–23]. This use of CeO_2 has been a result of its remarkable structural and chemical properties, which enhance the dispersion of the active metals, to improve the stability of the Al_2O_3 support, and to alter the interaction between the metal and the support. In recent studies of glycerol steam reforming, ceria added onto the Al_2O_3 support of Ni catalysts improved both of the catalytic activity in terms of the glycerol conversion, and the physicochemical properties of the catalyst by stabilizing the Ni phase, and inhibiting the formation of coke and NiAl_2O_4 [1,10,12,13,15]. Adhikari et al. [10], performed the glycerol SR over several noble metals (Ni, Pt, Rh, Pd, Ir, Ru) on Al_2O_3 and $\text{CeO}_2/\text{Al}_2\text{O}_3$ supports to find that CeO_2 greatly improved the activity of $\text{Rh}/\text{Al}_2\text{O}_3$. As a catalytic promoter, ceria improves the stability of the active Ni phase [1] and retards the formation of inactive NiAl_2O_4 species [12]. Buffoni et al. [13] reported that $\text{Ni}/\alpha\text{-Al}_2\text{O}_3$ modified by CeO_2 inhibits the secondary dehydration reactions that generate unsaturated hydrocarbons and coke precursors, thereby causing the deactivation of the catalyst. According to Iriondo et al. [15], CeO_2 promoter loading has a significant influence on the behavior of $\text{Ni}/\text{Al}_2\text{O}_3$ in glycerol SR. Only low CeO_2 loading (5–10%) improves the activity of the catalyst. The enhancement of the activity of $\text{Ni}/\text{Al}_2\text{O}_3$ by CeO_2 in the steam reforming of a glycerol-ethanol mixture was confirmed. Also, the performance of $\text{Ni}/\text{Al}_2\text{O}_3$ was better than that of $\text{Pt}/\text{Al}_2\text{O}_3$ [24].

In all previous studies of GSR over $\text{Ni}/\text{CeO}_2/\text{Al}_2\text{O}_3$, all promoted $\text{CeO}_2/\text{Al}_2\text{O}_3$ supports had been prepared by impregnating a ceria precursor on a commercial $\gamma\text{-Al}_2\text{O}_3$ support. No previous GSR work has used Ni-based catalysts supported on $\text{CeO}_2/\text{Al}_2\text{O}_3$ derived by a sol-gel method, even though the method supports well-developed mesoporous structures of uniform pore sizes, high homogeneity for several components during synthesis, a high surface area, and high catalytic activity [25–30]. Moreover, an inclusive comparison between preparation methods has not yet been done on the structural characteristics of $\text{CeO}_2/\text{Al}_2\text{O}_3$ mixed oxides and the catalytic behavior in GSR over nickel catalysts on $\text{CeO}_2/\text{Al}_2\text{O}_3$ supports. This study investigated the effects of preparing $\text{CeO}_2/\text{Al}_2\text{O}_3$ by a single-step sol-gel and impregnation method on the physico-chemical and structural properties of the mixed oxides and the Ni-supported catalysts. The catalytic activity, gas product selectivity, and coke resistance of the Ni catalysts supported on the oxides, towards the steam reforming of glycerol were studied. The $\text{CeO}_2/\text{Al}_2\text{O}_3$ supports and $\text{Ni}/\text{CeO}_2/\text{Al}_2\text{O}_3$ catalysts were comprehensively characterized by several techniques.

2. Experimental procedure

2.1. Catalyst preparation

The two alumina supports used to prepare the catalysts were commercial Al_2O_3 (Japan Chemicals) and a sol-gel derived alumina or xerogel, denoted as "Al.C" and "Al.S", respectively. The Al_2O_3 xerogel was prepared by first dissolving an alumina precursor, aluminum tri-sec-butoxide ($\text{Al}(\text{OCH}(\text{CH}_3)\text{C}_2\text{H}_5)_3$ or ASB (97% purity, Aldrich) in ethanol (99.9% purity, QRëC) with vigorous stirring and heated up to 80 °C. Next, nitric acid (67% solution, QRëC) was gently

added into the mixed solution for partially hydrolyzing the aluminum precursor, and a clear sol was subsequently obtained. After the sol was cooled down to room temperature, deionized water was added, and transparent gel formed within a few minutes. Then, the gel was aged, dried at 120 °C for 3 h and calcined at 800 °C for 3 h to yield the Al_2O_3 xerogel. It was denoted as "Al.S" and used as a support for loading ceria promoter in the next step.

Three $\text{CeO}_2/\text{Al}_2\text{O}_3$ mixed oxides at 10 wt% CeO_2 were prepared by two methods, impregnation and sol-gel. For impregnation method, both Al.C and Al.S were the supports impregnated with cerium nitrate precursor ($\text{Ce}(\text{NO}_3)_3 \cdot 6\text{H}_2\text{O}$, 99% purity (Aldrich Chemistry)). As described in the literature [31,32], the slurry of alumina powder and cerium nitrate solution was stirred vigorously overnight. After that, the impregnated slurry was dried and calcined at the same condition as shown above (120 °C for 3 h and 800 °C for 3 h, respectively). The promoted supports prepared from "Al.C" and "Al.S" were denoted as "CeAl.IC" and "CeAl.IS", respectively. The third $\text{CeO}_2/\text{Al}_2\text{O}_3$ support was prepared via the single-step sol-gel method which was done by making two separate solutions of the ASB and the cerium nitrate in ethanol. Then, they were vigorously mixed and stirred. As with the hydrolysis of the cerium-alumina precursors, gelation, drying and calcination procedures were followed using the same condition as above. The calcined $\text{CeO}_2/\text{Al}_2\text{O}_3$ powder obtained via this single-step sol-gel method was designated as "CeAl.SS".

The Ni catalysts supported on all the $\text{CeO}_2/\text{Al}_2\text{O}_3$ supports were prepared via the impregnation method following the procedure and condition described in our previous work [31,32]. The Ni at 15 wt% was added into the $\text{CeO}_2/\text{Al}_2\text{O}_3$ supports by using $\text{Ni}(\text{NO}_3)_2 \cdot 6\text{H}_2\text{O}$, (97% purity, QRëC) as the metal precursor. The paste of the Ni-based catalyst powder obtained were then dried and calcined at the same condition as that of the supports. The $\text{Ni}/\text{CeO}_2/\text{Al}_2\text{O}_3$ catalysts prepared using CeAl.IC, CeAl.IS and CeAl.SS supports were labeled as "NiCeAl.IC", "NiCeAl.IS" and "NiCeAl.SS", respectively.

2.2. Catalyst characterization

2.2.1. N_2 adsorption-desorption

The surface area of the catalysts was measured with an Autosorb I analyzer (Quantachrome) by applying the Brunauer-Emmett-Teller (BET) method of N_2 physisorption at the temperature of the liquid nitrogen (77 K), while the pore size distributions of all the catalysts were determined by the Barret-Joyner-Halender (BJH) method, as applied to the desorption branch of the nitrogen isotherm. Prior to the measurements, all the supports and the catalysts were sieved, and those with sizes of less than 250 μm were evacuated at 120 °C for 3 h to ensure that there was no adsorbed moisture on the surface of the catalysts, which were then reduced by flowing H_2 gas (99.99%, Praxair Thailand) at 700 °C for 3 h. Following the reduction, the catalysts were subsequently flushed under He (99.99%, Praxair Thailand) until cooling down to room temperature and were collected in the container kept in the desiccator cabinet in order to avoid exposing the reduced catalysts to air.

2.2.2. H_2 chemisorption

The amount of active Ni sites and the Ni dispersion on the catalyst surface were calculated from the H_2 -chemisorption data obtained using pulse chemisorption technique on a Micrometric Chemisorb 2720. Prior to the analysis, 0.1 g of the catalyst was reduced in H_2 flow at 700 °C for 3 h, and subsequently cooled in H_2 stream down to 400 °C and flushed with N_2 , each for 1 h. After that, the temperature was decreased to 100 °C for chemisorption analysis. The amount of H_2 consumed was determined by periodically injecting 0.1 μL of 99.99% H_2 onto the sample and repeating

at an interval of 10 min until the successive consumption peaks exhibited the same area. A chemisorption stoichiometry H:Ni of 1:1 and a cross-sectional area of Ni of $6.494 \times 10^{-20} \text{ m}^2 \text{ Ni-atom}^{-1}$ were assumed in the calculation.

2.2.3. X-ray diffraction

The X-ray diffraction (XRD) spectra of all the promoted supports and catalysts were obtained by using a Phillips PW 1830 equipped with CuK α source radiation ($\lambda = 0.1538 \text{ nm}$). The powder sample was sieved for particles with sizes less than 250 μm and it was dried at 120 $^{\circ}\text{C}$ for 3 h to remove the moisture before analysis. The fresh catalysts were reduced under H₂ gas flow at 700 $^{\circ}\text{C}$ for 3 h and were kept in the desiccator cabinet. Bragg angles between 10 $^{\circ}$ to 100 $^{\circ}$ were scanned at a rate of 0.05 $^{\circ}$ (2 θ) s^{-1} . The mean crystallite diameters of Ni and CeO₂ were calculated, using Scherrer's equation, from the XRD peaks at 2 θ of 51.8 $^{\circ}$ (200) and 28.6 $^{\circ}$ (111) for Ni and CeO₂, respectively.

2.2.4. H₂ temperature-programmed reduction

Hydrogen-temperature-programmed reduction (H₂-TPR) was performed to investigate the interaction between nickel species and supports, and the reducibility of the catalysts. The characterization was conducted by using a Quantachrome apparatus (ChemBET 3000). In each measurement, 0.1 g of a sample was reduced in a stream of a 10% H₂/N₂ mixture. The temperature of the sample was then increased from 50 $^{\circ}\text{C}$ to 900 $^{\circ}\text{C}$ at a ramping rate of 10 $^{\circ}\text{C min}^{-1}$. The H₂ consumption as a function of temperature was monitored by a thermal conductivity detector (TCD) cell.

2.2.5. NH₃-Temperature programmed desorption

Surface acidity of the samples was measured by temperature-programmed desorption of ammonia (NH₃-TPD) on a Chemisorb 2720 chemisorption analyzer (Micromeritics). The Ni/CeO₂-Al₂O₃ samples were *ex situ* reduced at 700 $^{\circ}\text{C}$ for 3 h under H₂ atmosphere. It was then placed into a quartz reactor and was pretreated in He flow at 200 $^{\circ}\text{C}$ for 30 min prior to NH₃ adsorption. Upon cooling to room temperature, the sample was then saturated by an NH₃ stream containing 15 vol% NH₃ in He (Linde Thailand) at 110 $^{\circ}\text{C}$ for 1 h. Then the weakly adsorbed NH₃ was subsequently removed by flushing with He (99.99% purity) until the baseline was stabilized. The NH₃-TPD analysis was carried out with a temperature ramp of 10 $^{\circ}\text{C min}^{-1}$ from 30 to 700 $^{\circ}\text{C}$ in a He flow at 20 mL min^{-1} . The desorption profile was monitored by a TCD cell and normalized by mass of the sample.

2.2.6. X-ray absorption near edge structure

X-ray absorption near edge structure (XANES) measurement was recorded in the transmission mode at the Ni K edge and the Ce L_{III} edge at the Beamline 8 of the Synchrotron Light Research Institute, Thailand. The Ge (220) crystal was used as a fixed-cut double crystal monochromator (DCM) for selecting the high X-ray energy range from the synchrotron radiation (1.2 GeV). The mixture of helium and argon gas was pumped into the ion chambers installed in front of and behind the sample in which the incident (I₀) and the transmitted (I₁). X-ray beams were continuously detected. Each sample was spread on the sample frame and sealed with Kapton windows.

2.2.7. X-ray photoelectron spectroscopy

The surface chemical composition and oxidation state of the samples were characterized by an X-ray photoelectron spectroscopy (XPS) technique. Photoelectron spectra were performed using an AXIS Ultra DLD (Kratos Analytical) electron spectrometer equipped with an Al K α monochromatic X-ray radiation source ($\hbar\nu = 1486.69 \text{ eV}$) at a power of 150 W. A hemisphere photoelectron analyzer operated at constant pass energies of 80 eV and 20 eV

for the survey and the high resolution scans, respectively. The catalysts were reduced *ex-situ* at 700 $^{\circ}\text{C}$ under flowing H₂ gas for 3 h and were preserved in a desiccator cabinet. The sample was outgassed before transferring the XPS sample holder to the ion-pumped analysis chamber for data acquisition under $3 \times 10^{-10} \text{ mbar}$. The peak of C 1 s located at the peak binding energy of 284.6 eV was used as an internal reference to correct all spectra.

2.2.8. Thermogravimetric analysis

The thermogravimetric analysis (TGA) was used to determine the change in weight due to coke deposited on the catalyst in relation to the change in temperature. The TGA analysis of the spent catalysts was performed by using a Pyris 1 TGA (PerkinElmer). Approximately 10 mg of each sample was evacuated to remove the moisture before being placed in a holder. The sample weight was recorded under heating from a room temperature to 110 $^{\circ}\text{C}$, and maintained for 10 min before heating it to 900 $^{\circ}\text{C}$ in flowing O₂ at 60 mL min^{-1} with a heating rate of 10 $^{\circ}\text{C min}^{-1}$. The amount of coke deposited was calculated and presented in a unit of $\text{mmol C gCat}^{-1} \text{ h}^{-1}$.

2.3. Catalytic reforming of glycerol

The catalytic activity of the Ni-based catalysts in glycerol steam reforming was performed in a fixed bed reactor, operated isothermally at 700 $^{\circ}\text{C}$ with a steam-to-glycerol molar ratio of 9, and a gas hourly space velocity (GHSV) of 42,000 h^{-1} . Prior to the reforming reaction, the catalyst was reduced *in situ* at 700 $^{\circ}\text{C}$ by flowing H₂ gas of 40 mL min^{-1} for 3 h. The glycerol solution (prepared from 99.5% glycerol (QR $\ddot{\text{e}}$ C)) was then introduced into the pre-heater controlled at 300 $^{\circ}\text{C}$ by using a HPLC pump (Eldex) with a flow rate of 0.1 mL min^{-1} before the solution entered the reactor. High purity (99.99%) He was used as the carrier gas. The outlet gas stream from the reactor was immediately cooled to condense and separate the liquid product. The gas product was collected and subsequently analyzed by a gas chromatograph (Shimadzu GC-14B) equipped with a thermal conductivity detector (TCD) and a flame ionization detector (FID). H₂, CO, and CH₄ were detected by using a Molecular Sieve 13X column, whereas a Porapak Q column was used for determining CO₂, CH₄ and C₂ hydrocarbons in the gas product.

The condensed liquid products were qualitatively analyzed by a gas chromatograph–mass spectrometer (GC–MS). A gas chromatograph (Clarus[®] 680, Perkin Elmer) provides with a 30 m \times 0.25 mm Elite-WAX ETR capillary column and is directly connected with a mass spectrometer (Clarus[®] SQ8T) detector. He (99.999%) was used as a carrier gas at a constant flow rate of 2 mL min^{-1} . The temperature was kept constant at 40 $^{\circ}\text{C}$ for 5 min, then it was increased to 250 $^{\circ}\text{C}$ at a heating rate of 10 $^{\circ}\text{C min}^{-1}$. The *m/z* was fully scanned from 29 to 120 under electron impact ionization at 70 eV. The temperatures of both the injector and the FID detector were kept constant at 250 $^{\circ}\text{C}$. 1 μL of sample was injected with a split ratio of 100:1.

The activity of each catalyst was generally reported in terms of the conversions of the glycerol into gas phase (X_{Gly}), the product yield (Y_i), and the product selectivity (S_i), as formulated in the following equations:

$$X_{\text{Gly}} (\%) = \frac{\text{moles of total C atoms in gas product}}{\text{moles of C atoms in feed}} \times 100 \quad (1)$$

For the H₂ gas product:

$$Y_{\text{H}_2} (\%) = \frac{\text{moles of H}_2 \text{ in gas product}}{7 \times \text{moles of glycerol in feed}} \times 100 \quad (2)$$

$$S_{\text{H}_2} (\%) = \frac{\text{moles of H}_2 \text{ in gas product}}{\text{moles of C atoms in gas product}} \times \frac{1}{\text{RR}} \times 100 \quad (3)$$

where RR is the reforming ratio of H_2 to CO_2 and is equal to 7/3 based on the stoichiometry of the glycerol steam reforming, as presented in Eq. (4):



For CO , CO_2 and hydrocarbons (i):

$$Y_i (\%) = \frac{\text{moles of species } i \text{ in gas product}}{\text{moles of C atoms in feed}} \times 100 \quad (5)$$

$$S_i (\%) = \frac{\text{moles of species } i \text{ in gas product}}{\text{moles of C atoms in gas product}} \times 100 \quad (6)$$

3. Results and discussion

3.1. Characterization of the supports and catalysts

3.1.1. Physical properties

The nitrogen adsorption-desorption isotherms and pore size distributions of the Al_2O_3 and $CeO_2-Al_2O_3$ supports, and the $Ni/CeO_2-Al_2O_3$ catalysts are shown in Fig. 1. The $CeO_2-Al_2O_3$ supports and the catalysts supported on $CeO_2-Al_2O_3$ exhibited the same type IV isotherm, the characteristic of mesoporous solids, as that of the pure Al_2O_3 supports but with different hysteresis loops of pore structure. The supports and the Ni supported on the commercial alumina ($Al.C$, $CeAl.IC$ and $NiCeAl.IC$) had H3-type hysteresis loop showing the “slit-shaped” pore structure. On the other hand, those based on sol-gel alumina ($Al.S$, $CeAl.SS$, $CeAl.IS$, $NiCeAl.IS$ and $NiCeAl.SS$) yielded H2-type hysteresis loops indicating the existence of the “ink-bottle” pore structure, narrow pore mouth and large cavity. The detailed physical properties of Al_2O_3 , $CeO_2-Al_2O_3$ and Ni catalysts are summarized in Table 1. The $Al.S$ shows smaller pore volume and average pore size diameter with narrower pore size distribution than does the $Al.C$ (4–15 nm vs. 4–30 nm). It can be explained by the nature of the pore formation of the Al_2O_3 supports prepared from different methods. The pores of the $Al.C$ support was formed by the aggregation of nanoparticles [27,33] while the $Al.S$ pores were composed of initiating links between the sol particles forming a three-dimensional solid network [34]. Hence, the pore size distributions of the promoted supports follow those of the pure alumina supports; $CeAl.SS$ and $CeAl.IS$ oxides in the range of 3–15 nm and 2–17 nm, respectively, 4–30 nm for $CeAl.IC$. These results reflect the more well-developed mesoporous structure of the sol-gel-based oxides over the conventional-based oxide.

After impregnating CeO_2 promoter into both $Al.C$ and $Al.S$ supports, the BET surface areas of the $CeAl.IC$ and $CeAl.IS$ promoted supports were severely reduced (from 220 to 167 $m^2 g^{-1}$ and 241 to 137 $m^2 g^{-1}$, respectively) as the small and some large pores had been blocked and partially filled with the CeO_2 promoter. On the other hand, incorporating cerium onto the alumina structure of $CeAl.SS$ prepared by sol-gel method caused a significant decrease in surface area of the promoted xerogel support (from 241 to 200 $m^2 g^{-1}$). Impregnation of Ni component over the $CeO_2-Al_2O_3$ mixed oxides further decreased the surface area of all the

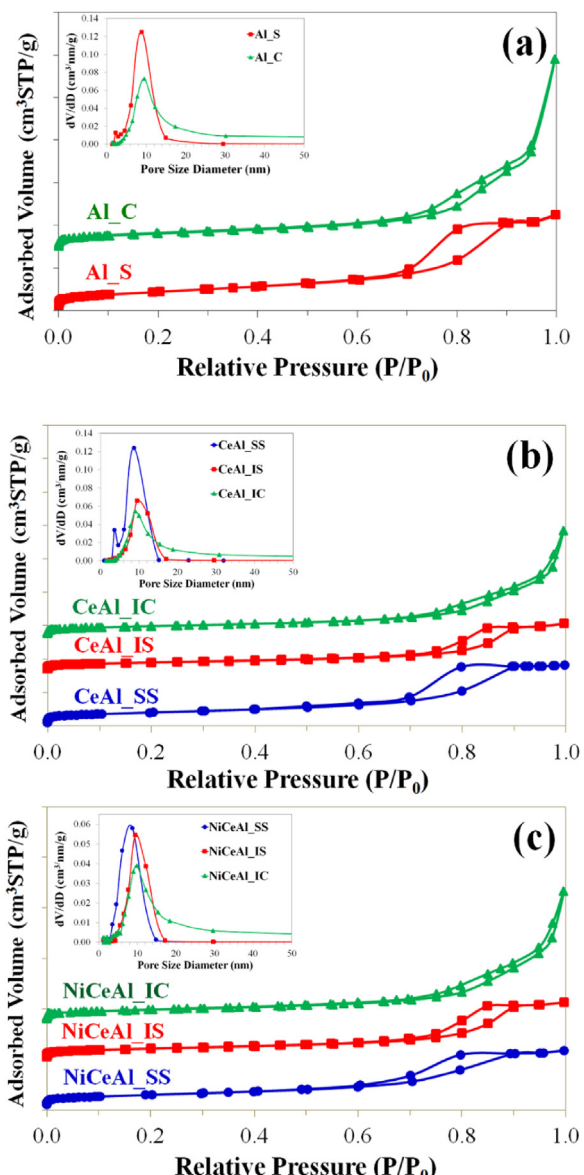


Fig. 1. Nitrogen adsorption-desorption isotherms and pore size distribution of (a) Al_2O_3 , (b) $CeO_2-Al_2O_3$ supports and (c) reduced $Ni/CeO_2-Al_2O_3$ catalysts.

catalysts because of the coverage over the internal support surface and the pore blockage by nickel species. Among these catalysts the $NiCeAl.SS$ had the highest value of 141 $m^2 g^{-1}$ followed by $NiCeAl.IS$ and $NiCeAl.IC$ (131 and 129 $m^2 g^{-1}$), respectively.

3.1.2. Crystalline structures of supports and Ni-based catalysts

The crystalline phases of all the calcined oxides examined by XRD are illustrated in Fig. 2(a). The reflections at 2-theta of 37.7°,

Table 1

Textural properties of the supports and the catalysts resulted from N_2 isotherms, and Ni dispersion on the catalysts from H_2 -chemisorption.

Supports/Catalysts	BET surface area ($m^2 g^{-1}$)	Pore Volume ($cm^3 g^{-1}$)	Average Pore Diameter (nm)	Number of active sites ($atom g^{-1}$)	Ni Dispersion (%)
Al.S	241	0.66	11.0	–	–
Al.C	220	1.35	24.6	–	–
CeAl.SS	200	0.53	10.0	–	–
CeAl.IS	137	0.44	12.5	–	–
CeAl.IC	167	0.95	22.8	–	–
NiCeAl.SS	141	0.33	9.4	2.20×10^{18}	1.41
NiCeAl.IS	131	0.38	11.5	2.14×10^{18}	1.28
NiCeAl.IC	129	0.78	23.8	1.20×10^{18}	0.75

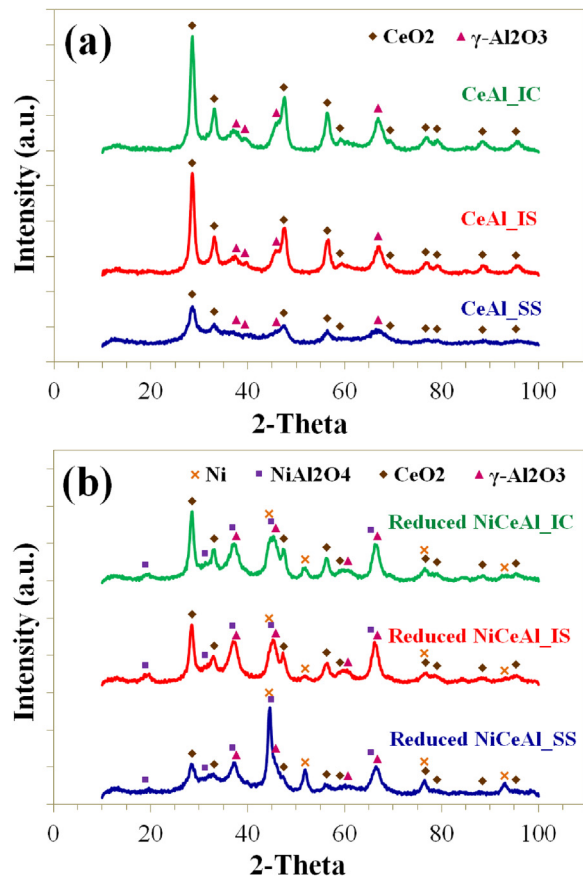


Fig. 2. XRD patterns of (a) CeO₂-Al₂O₃ supports after calcination at 800 °C and (b) Ni/CeO₂-Al₂O₃ catalysts after reduction at 700 °C.

39.4°, 45.8°, and 66.8° were identified as the γ-Al₂O₃ phase (JCPDS 79-1558), and those at 28.6°, 33.1°, 47.5°, 56.3°, 59.1°, 69.4°, 76.7°, 79.1°, 88.4°, and 95.4°, which belong to the cubic phase of CeO₂ (JCPDS 34-0394), were detected in all the promoted supports. The calculated CeO₂ crystal size (6.5 nm) of the CeAl_SS is considerably smaller than those of CeAl_IS (9.0 nm) and CeAl_IC (8.6 nm), as summarized in Table 2. It is also interesting to note that both CeAl_IS and CeAl_IC exhibited much higher intensity in the CeO₂ crystalline than did the one prepared by the single step sol-gel method, although all the mixed oxides had the same ceria loading. This is an indication of the formation of a well-dispersed CeAlO₃ species on the CeAl_SS.

Fig. 2(b) presents the XRD patterns of all the reduced Ni/CeO₂-Al₂O₃ catalysts and shows the peaks at 2-theta of 44.5°, 51.8°, 76.3°, and 92.9° corresponding to the Ni phase (JCPDS 04-0850). Also they all have the reflections at 19.1°, 31.4°, 37.0°, 45.0°, 65.5°, and 77.7° corresponding to the NiAl₂O₄ phase (JCPDS 10-0339). The presence of the NiAl₂O₄ phase arises from the incorporation of the NiO phase into the γ-Al₂O₃ phase and can be substantiated

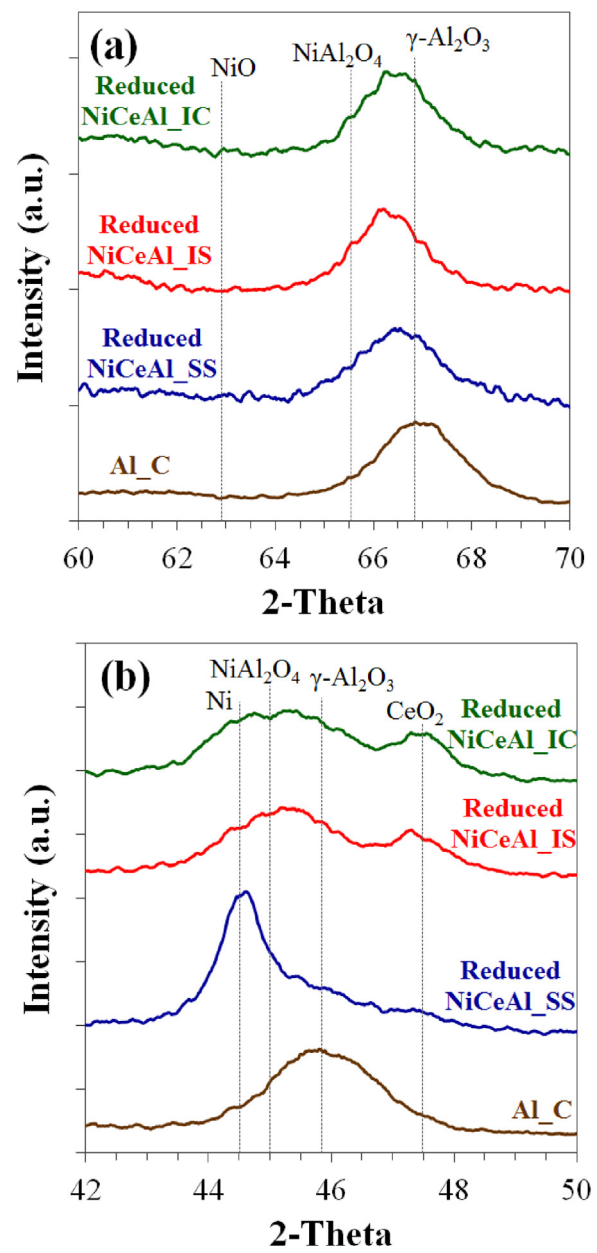


Fig. 3. XRD patterns for calcined commercial Al₂O₃ (Al.C) and reduced Ni/CeO₂-Al₂O₃ (NiCeAl_SS, NiCeAl_IS and NiCeAl_IC) in the 2-theta range of (a) 60–70° and (b) 42–50°.

from two indications: (i) the relative intensity of the main reflection peaks (37° and 45°) commonly appear in both γ-Al₂O₃ and NiAl₂O₄ according to JCPDS 79-1558 (γ-Al₂O₃) and JCPDS 10-0339 (NiAl₂O₄) [35], and (ii) the shift of the maximum reflection peak of Al₂O₃ (440) from 2-theta of 66.8° to the lower angle of 66.3° for both NiCeAl_IS and NiCeAl_IC, and 66.5° for NiCeAl_SS, as illustrated in Fig. 3(a). A further explanation for the former indication could be given regarding the relative intensities of the peaks at 37° to 45° for the γ-Al₂O₃ and the NiAl₂O₄, which are 0.69 and 1.54, respectively. The ratios for NiCeAl_IS and NiCeAl_IC were found to be 0.96 and 0.83 which are in-between those of γ-Al₂O₃ and NiAl₂O₄. However, for the NiCeAl_SS catalyst, the ratio was at 0.37, which is much lower than those of both phases. Further consideration was given to the peaks corresponding to the Ni phase especially at the 2-theta range of 43°–46°, as shown in Fig. 3(b). The NiCeAl_SS catalyst obviously shows the Ni phase at 44.5° whereas a broad peak starting from 43.2° to 46.7° was observed for NiCeAl_IS and

Table 2

Average size of Ni and CeO₂ crystals of the promoted supports, and reduced and spent catalysts.

Supports/Catalysts	CeO ₂ crystal (nm)	Ni crystal (nm)	
		Reduced	Spent
CeAl_SS	6.5	–	–
CeAl_IS	9.0	–	–
CeAl_IC	8.6	–	–
NiCeAl_SS	6.6	8.4	11.6
NiCeAl_IS	8.6	8.2	10.9
NiCeAl_IC	8.7	6.9	14.7

NiCeAl_IC, indicating the existence of the NiAl_2O_4 phase in both catalysts. From crystal size estimation using Scherrer's equation, the Ni crystallite sizes of the NiCeAl_SS and NiCeAl_IS catalysts are larger than that of the NiCeAl_IC catalyst, as listed in Table 2. The peaks corresponding to CeO_2 structure were also observed in all the catalysts and the reduced NiCeAl_SS had the least relative intensity of the CeO_2 , which is similar to what was observed for the promoted support. In addition, the CeO_2 crystal sizes for all the reduced catalysts were found nearly unchanged, showing that the impregnation of the nickel precursor onto the $\text{CeO}_2\text{-Al}_2\text{O}_3$ supports had had an insignificant influence on the crystallite size of the CeO_2 . It is possible that there was no or little interaction between nickel and ceria as Ni^{2+} is not favored to integrate in the ceria structure, because of the too small ionic radius in VIII coordination [36], whilst the nickel species was well dispersed on the supports.

3.1.3. Metal dispersion

The number of active sites and Ni dispersion results of all the reduced catalysts determined by H_2 -pulse chemisorption measurement are given in Table 1. It is shown that NiCeAl_SS has the highest number of active sites and metal dispersion which are slightly higher than those of NiCeAl_IS, and almost twice of NiCeAl_IC. This is because of the higher amount of the easily reducible nickel species on the NiCeAl_SS than that on the NiCeAl_IS and NiCeAl_IC catalysts as shown in the XRD results, and the higher surface area of the sol-gel based oxides. It is anticipated that ceria incorporated into alumina structure during the sol-gel preparation thereby lowering the interaction between nickel and alumina. This result is in agreement with that of the XRD.

3.1.4. Reducibility of the $\text{CeO}_2\text{-Al}_2\text{O}_3$ and the Ni-based catalysts

The H_2 -TPR of the promoted supports and the Ni catalysts are shown in Fig. 4(a) and (b), respectively. Five temperature regions, located at below 300 °C, 300–480 °C, 480–620 °C, 620–790 °C and above 790 °C, were observed in the TPR profiles of all the $\text{CeO}_2\text{-Al}_2\text{O}_3$ supports, which are in accordance with the literature [12,25,37,38]. The broad peak observed below 300 °C, which is much in evidence for the CeAl_SS support, corresponded to the removal of the moisture physisorbed on the support [39] and the oxygen adsorption on the Al_2O_3 [37,40]. The regions in the medium temperature ranges of 300–480 °C and 480–620 °C are related to the elimination of the surface oxygen atoms on the small CeO_2 crystallites [25,38,41] and the formation of the non-stoichiometric CeO_x phase, respectively [38,39,42]. Subsequently, the surface of the residual ceria that had been in more contact with the Al_2O_3 surface was reduced to form superficial CeAlO_3 with the replacement of the Ce^{3+} cations in the Ce_2O_3 species that had been formed into the first layer of the Al_2O_3 during the prolonged reduction, which corresponded to the peak in the range of 620–790 °C [37,38]. The last region, which is above 790 °C, represents the removal of the oxygen atoms located in large bulk CeO_2 crystallites [25,37,38,41].

For CeAl_IC support, the reduction peaks were observed in wide temperature regions with the maximum peaks centered at 394 °C, 590 °C, 739 °C, and 880 °C as shown in Fig. 4(a). The CeAl_SS support had small and broad reduction peaks ranging from 350 °C to 880 °C with the maximum peaks centered at 444 °C, 603 °C, 788 °C, and 856 °C. The very low intensity of the peaks for the CeAl_SS support could be attributed to the reduction of the much smaller sizes of CeO_2 and the formation of well-dispersed CeAlO_3 , which is consistent with the XRD results. Contrary to what was observed for the CeAl_IC and CeAl_SS supports, the TPR profile for the CeAl_IS clearly shows the reduction peak in the medium to high-temperature regions with a maximum at 867 °C, accompanied by a broad shoulder at 474 °C, 619 °C, and 765 °C. Moreover, the latter peaks in the high-temperature region that are the characteristics of the bulk ceria reduction for the CeAl_IS and CeAl_IC supports prevailed con-

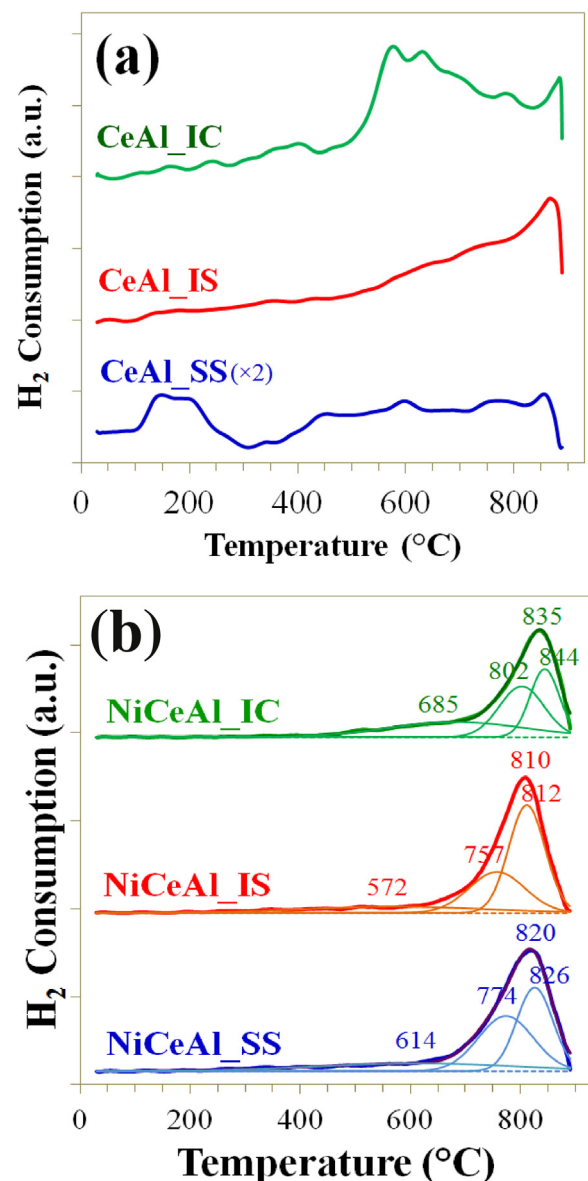


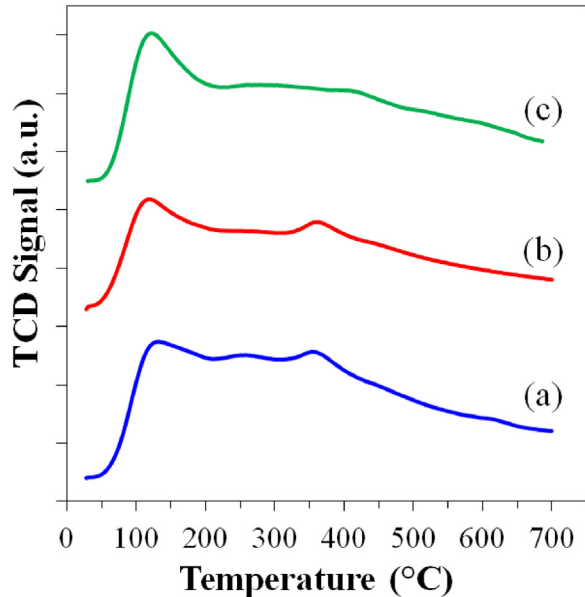
Fig. 4. TPR profiles of (a) $\text{CeO}_2\text{-Al}_2\text{O}_3$ supports and (b) fresh $\text{Ni}/\text{CeO}_2\text{-Al}_2\text{O}_3$ catalysts obtained from original profiles and deconvoluted profiles.

siderably over that of the CeAl_SS support. These results suggest that the CeAl_IS and CeAl_IC supports had more portions of large CeO_2 crystallite size than did the CeAl_SS support [25], which is consistent with the XRD results presented in Table 2. In other words, the reducibility of the supports increases with decreasing crystallite size of CeO_2 . The similar finding has been reported for TiO_2 used as a support for Pt catalyst in water-gas-shift reaction [43].

The TPR profiles of the NiCeAl_SS, NiCeAl_IS and NiCeAl_IC catalysts exhibit similar broad reduction bands with maximum temperatures of 820 °C, 810 °C and 835 °C, respectively, as illustrated in Fig. 4(b). By performing curve-fitting and Gaussian multiple peaks deconvolution using Origin software, the three peak components of the reducible species and their corresponding area percentages were obtained as shown in Fig. 4(b) and summarized in Table 3, respectively. The first peak appearing at a temperature below 650 °C is the reduction peak of NiO interacting with Al_2O_3 support [15,35,44]. The second and the third reduction peaks, with the maximum peaks at 760–800 °C and above 820 °C, are ascribed to the reduction of the non-stoichiometric nickel aluminate species (NiAl_xO_y) and the stoichiometric species of NiAl_2O_4 , respectively

Table 2. Oxidation state of Ce.Relative proportion and reduction temperature of catalysts, and amount of NH_3 desorbed of the reduced catalysts.

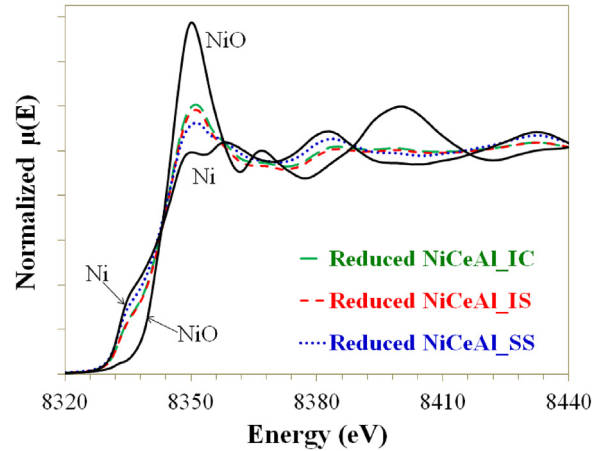
Catalysts	$\text{NiO-Al}_2\text{O}_3$	NiAl_xO_y	NiAl_2O_4	NH_3 desorbed amount ($\mu\text{mol g}_{\text{Cat}}^{-1}$)
NiCeAl_SS	20.0% (614 °C)	40.0% (774 °C)	40.0% (826 °C)	4219
NiCeAl_IS	14.9% (572 °C)	31.3% (757 °C)	53.8% (812 °C)	3015
NiCeAl_IC	32.0% (685 °C)	36.2% (802 °C)	31.8% (844 °C)	3822

**Fig. 5.** NH_3 -TPD desorption profiles of the catalysts (a) NiCeAl_SS, (b) NiCeAl_IS, and (c) NiCeAl_IC.

[12,33]. The Gaussian deconvolutions for the reducible species of the $\text{CeO}_2\text{-Al}_2\text{O}_3$ supports were ignored because of the inconsiderable amount of $\text{CeO}_2\text{-Al}_2\text{O}_3$ reduction when compared to the amounts of $\text{Ni/CeO}_2\text{-Al}_2\text{O}_3$ reduction. The NiCeAl_SS catalyst shows three reduction peaks with maximum temperatures at 614 °C, 774 °C and 826 °C, whereas the maximum peaks at 572 °C, 757 °C, and 812 °C were observed for the NiCeAl_IS catalyst. Although the peaks of NiCeAl_IS had shifted to lower temperatures, the proportion of the reducible $\text{NiO-Al}_2\text{O}_3$ species of the NiCeAl_SS catalyst was larger than that of the NiCeAl_IS catalyst. By comparing with the NiCeAl_IC catalyst exhibiting the reduction peaks at the highest temperatures of 685 °C, 802 °C, and 844 °C, the $\text{NiO-Al}_2\text{O}_3$ species of the NiCeAl_SS and NiCeAl_IS catalysts are in smaller quantities but more easily reduced at lower temperatures than that of the NiCeAl_IC catalyst. In addition, the stoichiometric and non-stoichiometric nickel aluminate species (NiAl_2O_4 and NiAl_xO_y) of both NiCeAl_SS and NiCeAl_IS were present at much lower temperatures than those of NiCeAl_IC. This shows that the nickel species on the xerogel alumina support had retained higher reducibility than did the one on the commercial non-xerogel alumina. The higher reducibility was a result of the incorporation of ceria into the alumina prepared by the sol-gel method. These results are also in agreement with those of XRD.

3.1.5. Acidity of $\text{Ni/CeO}_2\text{-Al}_2\text{O}_3$ catalysts

The NH_3 -TPD was performed to obtain the concentrations of the acid sites as well as acidity of the catalysts. The TPD profiles are displayed in Fig. 5. The area under the peak was calibrated with a known quantity of NH_3 . Then, the amount of NH_3 adsorbed representing the surface acid site concentration of the catalysts can be calculated as summarized in Table 3. Three catalysts have similar ammonia desorption patterns with a broad shape in the temperature range of 30–700 °C, but with different acid site concentrations.

**Fig. 6.** XANES spectra of the Ni K-absorption edge for Ni foil (Ni^0), NiO (Ni^{2+}), reduced NiCeAl_SS, NiCeAl_IS, and NiCeAl_IC catalysts.

NiCeAl_SS shows the highest total amount of acid sites than do NiCeAl_IC and NiCeAl_IS. Furthermore, the catalysts supported on the sol-gel derived xerogel showed a high temperature peak at about 350 °C. These acid sites were contributed by the occurrence of CeAlO_3 species [45] whilst the typical impregnation method induces the formation of fewer CeAlO_3 perovskite structures. Guo et al. [30] also reported that the presence of higher temperature peaks on the $\text{CeO}_2\text{/Al}_2\text{O}_3$ catalyst prepared by the sol-gel method had resulted from the interaction between the Ce species and Al_2O_3 . The high temperature acid sites correspond to the Brønsted acid sites of the solid surface [30] and the strong Lewis acid sites contributed by Al_2O_3 [45,48], whereas the low temperature acid sites are weak acid sites and mainly contributed by CeO_2 [46] due to its generally weak basicity [47].

3.1.6. X-ray absorption near edge structure (XANES)

To investigate the change in the Ni and Ce oxidation states after reduction with flowing pure H_2 at 700 °C for 3 h, the electronic characters of the Ni and Ce atoms were explored by the XANES method. The XANES signals from the measured absorption spectra were extracted by the pre-edge background and were normalized by dividing the peak intensity by the height of the absorption edge. The data reduction was analyzed using the Athena software program.

3.1.6.1. Oxidation state of Ni.

Fig. 6 depicts the XANES spectra of the Ni K-absorption edge for the Ni standard, Ni^0 and NiO (Ni^{2+}), and the Ni samples, NiCeAl_SS, NiCeAl_IS and NiCeAl_IC catalysts. The XANES spectra of the NiO standard exhibited a small pre-edge peak due to the 1s-3d transition [12,49], and the white line of that sample was observed at 8350.2 eV. In contrast, the weak pre-edge peak at 8332.7 eV, or no white line, appertained to the Ni^0 standard. After the catalyst samples were reduced, a change in the adsorption edge energy and a decrease in the white line intensity were observed for all the reduced catalysts. This indicated that Ni^{2+} in all the catalysts had been converted to Ni^0 [12]. Additionally, the NiCeAl_SS had the highest reducibility, as its XAS profile was the closest to the Ni^0 standard. This was in agreement with the results of the TPR studies.

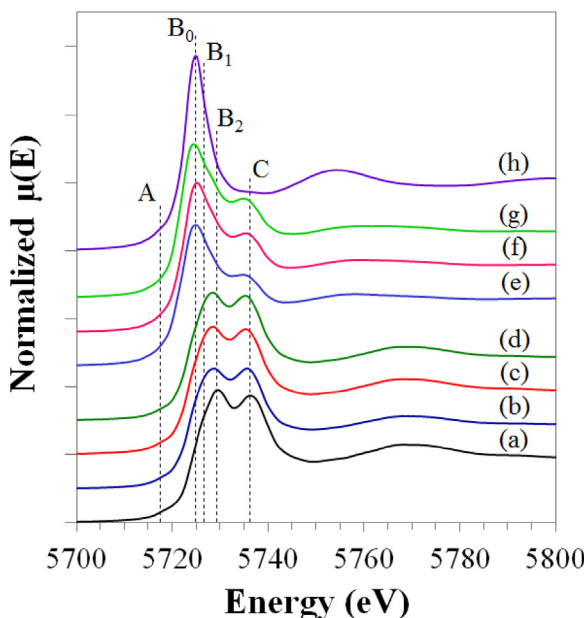


Fig. 7. XANES spectra of the Ce L_{III} absorption edge for (a) CeO₂ (Ce⁴⁺), fresh catalysts (b) NiCeAl.LS; (c) NiCeAl.IS; (d) NiCeAl.IC, reduced catalysts (e) NiCeAl.LS; (f) NiCeAl.IS; (g) NiCeAl.IC, and (h) Ce(NO₃)₃·6H₂O (Ce³⁺).

The XANES spectra of the Ce L_{III} edge of the Ce standard, CeO₂ (Ce⁴⁺) and Ce(NO₃)₃·6H₂O (Ce³⁺), the fresh and the reduced Ni/CeO₂-Al₂O₃ catalysts are illustrated in Fig. 7. The difference of XANES spectra between Ce⁴⁺ and Ce³⁺ is evidently presented as illustrated in Fig. 7(a) and (h), respectively. The Ce L_{III} edge XANES spectrum of CeO₂ exhibits two main detached peaks at 5729.4 and 5736.2 eV, labeled as B₂ and C, respectively. The appearance of these two peaks corresponds to the different final states of Ce caused by the hybridization of the 4f orbital of Ce and the 2p orbital of O. The first white line, B₂, occurs due to the electron transfer from the 2p orbital of O to the Ce 4f orbital, Ce [2p⁵4f¹5d^{*1}] O 2p⁵, while the second peak, C, was found because there was no electron contained in the 4f orbital of Ce and no holes in the 2p orbital of O, Ce [2p⁵4f⁰5d^{*1}] O 2p⁶. This is in good agreement with the results reported in the literatures [50–52]. Besides the two main peaks, a small pre-edge peak at 5717.6 eV, labeled as A, was also observed on CeO₂ (Ce⁴⁺), because of the transition of the unoccupied Ce d-state at the bottom of the conduction band or the dipole-forbidden 2p_{3/2} to 4f [51,53]. Although the energy shift of the pre-edge peak is often used to determine the oxidation states of the Ce species in samples, it was hardly observed here as it was too subtle. Moreover, the shoulder of the intense B₂ peak at 5726.7 eV ascribed to the final state transition of Ce [2p⁵4f¹5d^{*1}] O 2p⁵ was labeled as B₁. This shoulder peak was observed on Ce⁴⁺ compounds and other rare earth oxides with a fluorite structure [50]. In contrast to the XANES spectrum for CeO₂, the simple shape of Ce³⁺ absorption state was found, as only single white line at 5724.8 eV, noted as B₀, was observed, corresponding to the Ce [2p⁵4f¹5d^{*1}] O 2p⁶ final state [50,52–54]. The single strong absorption not only was observed on the Ce(NO₃)₃·6H₂O but also on all the Ce³⁺ compound, as investigated in the literatures [52,53].

The XANES spectra of the Ce L_{III} absorption edge for all the fresh Ni/CeO₂-Al₂O₃ catalysts were very similar to those of the CeO₂ spectra as shown in Fig. 7 ((b)–(d)). Moreover, the trivial change in the height of the edge jump at the white line observed in the fresh catalysts could have resulted from the differences in the particle sizes and morphologies of the catalysts [51]. After all the fresh catalysts had been reduced under H₂ atmosphere at 700 °C, the peaks, identified as B₂ and C, decreased, and a new white line noted as B₀

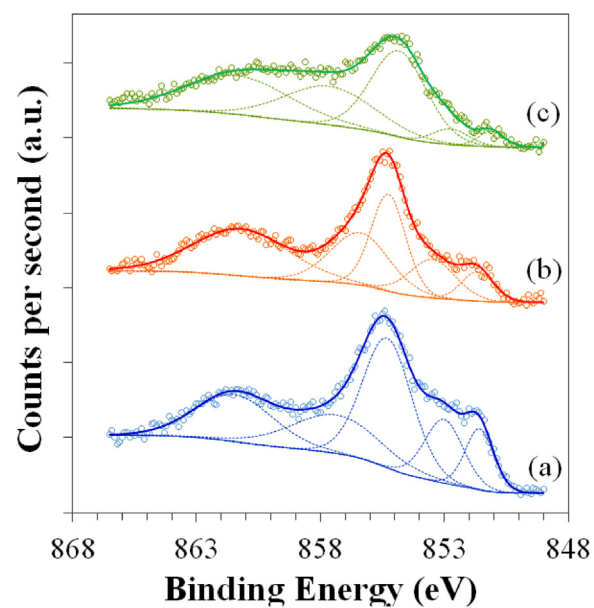


Fig. 8. XPS spectra of Ni 2p_{3/2} core level for reduced (a) NiCeAl.LS; (b) NiCeAl.IS; (c) NiCeAl.IC catalysts.

was observed (See Fig. 7 (e)–(g)). Nevertheless, the presence of CeO₂ was also detected, as the respective line labeled as C still appeared [54]. By comparison, the reduced NiCeAl.LS spectra contained the peak C, which was less intense than those of the reduced NiCeAl.IS and NiCeAl.IC catalysts. These results indicated that the NiCeAl.LS catalyst was more easily reducible than NiCeAl.IS and NiCeAl.IC catalysts.

3.1.7. X-ray photoelectron spectroscopy (XPS)

3.1.7.1. Ni/CeO₂-Al₂O₃ samples. As with the XAS analysis, the XPS technique was extended to all the reduced catalysts for determining the oxidation state of the Ni element and the surface composition of the Ni species in different chemical states. The X-ray photoelectron spectra of the Ni species for the reduced catalysts were fitted by Gaussian-Lorentzian curve-fitting done with the CasaXPS software program in order to determine the peak areas for obtaining the relative surface proportion of the Ni species after subtracting a Shirley background. The XPS spectra of the Ni 2p_{3/2} core-levels for the reduced catalysts are shown in Fig. 8, and the binding energies of each Ni species are summarized in Table 4. The XPS spectra for Ni 2p_{3/2} core-levels in all the reduced catalysts were deconvoluted into three peaks located at ~851.6, 853.0, and 855.3 eV, indicating the different oxidation states of Ni that corresponded to Ni⁰, Ni²⁺ from NiO weakly interacting with the Al₂O₃ support, and Ni²⁺ from the NiAl_xO_y and NiAl₂O₄ spinel structures, respectively [15,44,55]. Moreover, shake-up satellite peaks were observed at the binding energies of 857.4 and 861.5 eV, showing the existence of Ni⁰ and Ni²⁺ species, respectively [55]. It indicates that there was a mixture of metallic Ni and Ni²⁺ species on the surfaces of all the reduced catalysts, inferring that some of the surface Ni²⁺ species had hardly

Table 4

Binding energies of Ni 2p_{3/2} core-level for reduced catalysts.

Catalysts	Binding Energy Ni 2p _{3/2} (eV) ^a				
	Ni ⁰	Ni ²⁺ (NiO)	Ni ²⁺ (NiAl _x O _y)	Ni ⁰ (sat.)	Ni ²⁺ (sat.)
NiCeAl.LS	851.6 (17)	853.0 (23)	855.3 (60)	857.4	861.5
NiCeAl.IS	851.7 (16)	853.5 (29)	855.3 (55)	856.4	861.2
NiCeAl.IC	851.1 (7)	852.8 (10)	854.9 (83)	857.7	861.4

^a % Content of Ni species at different oxidation states on the catalyst surface.

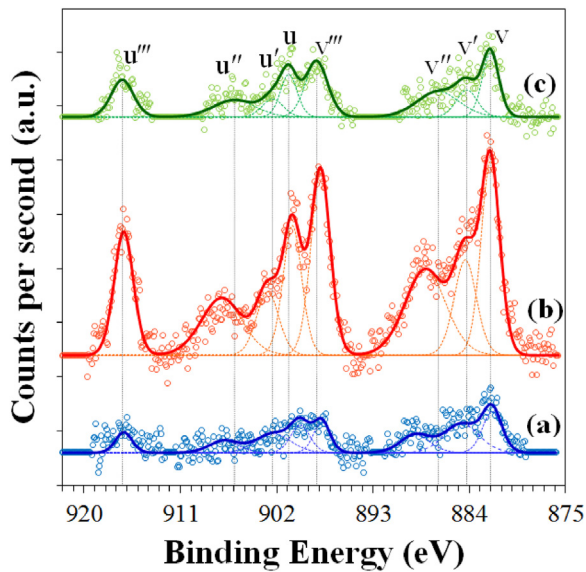


Fig. 9. XPS Ce 3d spectra for calcined (a) CeAl_{SS}, (b) CeAl_{IS}, and (c) CeAl_{IC} promoted supports.

been reduced into metallic Ni. This result is in agreement with the H₂-TPR study.

The relative proportions of different Ni species in the reduced catalysts were determined as listed in Table 4. After reduction, the divalent Ni strongly interacted with the Al₂O₃ support and formed NiAl₂O₄ which is the predominant species on the surfaces of all the reduced catalysts, especially the NiCeAl_{IC} catalyst. NiO which is the other Ni²⁺ form and easily reducible species was present the least in NiCeAl_{IC}, in the amount of less than half of those in NiCeAl_{IS} and NiCeAl_{SS}. Additionally, twice the amount of Ni⁰ was observed over the superficial NiCeAl_{SS} and NiCeAl_{IS} catalysts, as compared to that of the NiCeAl_{IC} catalyst. It is inferred that the NiCeAl_{SS} and the NiCeAl_{IS} catalysts had retained higher reducibility than the NiCeAl_{IC}. These results are in agreement with the XRD, TPR, and XAS results.

3.1.7.2. CeO₂-Al₂O₃ samples. Analysis of the XPS spectra of the Ce 3d core levels for all the Ni-based catalysts cannot distinguish the Ce 3d region from the Ni 2p region, because of the partial overlapping between Ni 2p_{1/2} and Ce 3d_{5/2} peaks located in binding energy range of ~870–890 eV. To elucidate the effects of the alumina texture and the CeO₂-Al₂O₃ support preparation methods on the surface chemical composition quantitatively, the CeO₂-Al₂O₃ supports were analyzed. The XPS spectra of the Ce 3d core electron levels for the calcined CeO₂-Al₂O₃ supports are depicted in Fig. 9. Three pairs of spin-orbit doublets were observed to fit into the six small peaks in the spectrum of CeO₂. The peaks labeled as v (882.0 eV), v'' (886.9 eV) and v''' (898.3 eV) are ascribed to the Ce 3d_{5/2} spin orbit component whereas the peaks present at 900.9 eV, 906.0 eV, and 916.4 eV corresponded to u, u'', and u''', respectively, belong to Ce 3d_{3/2} component [25,38,51,56,57]. Moreover, the satellite peak of Ce 3d_{3/2} (u'') at a binding energy of 916.4 eV is the characteristic of the transition from the Ce 3d¹⁰4f⁰ initial state into the Ce 3d⁹4f⁰ O 2p⁶ configuration or Ce⁴⁺ state [37,38,46,57]. Compared to CeO₂, not only the three pairs of spin-orbit doublets, but also the growth of the v' (884.2 eV) and u' (902.4 eV) peaks was found in the spectrum of Ce 3d for all the CeO₂-Al₂O₃ samples. These peaks are related to the Ce 3d⁹ 4f¹ O 2p⁶ configuration ascribed to the Ce³⁺ state. To verify the presence of the different oxidation states of Ce, the area percentage of the u'' peak (%u'') in the total Ce 3d region, Ce 3d_{5/2} and Ce 3d_{3/2}, is used to describe the relative

intensity of Ce⁴⁺ in the samples [37], as presented in Table 5. It was found that the values of the %u''' for all the CeO₂-Al₂O₃ supports were lower than that for the CeO₂ calcined at 800 °C which is 13.4% as reported in the work of Shyu et al. [37]. The lowest %u''' (~7.1%) was measured in the CeAl_{SS} support while it was 11.0% and 12.4% for CeAl_{IS} and CeAl_{IC}, respectively, close to that of CeO₂, suggesting that the Ce species on the Al₂O₃ support for CeAl_{SS} resembles Ce³⁺. This was due to the strong interaction between Ce and Al₂O₃ forming CeAlO₃ [37,38]. As it can be seen in Fig. 9, the appearance of v' and the diminution of the v component confirmed that the Ce configuration had crept into the Ce³⁺ ion state. The intensity ratios of v' and v (I(v'/v)), summarized in Table 5, show that the CeAl_{SS} support had the higher value of I(v'/v), as compared to that of CeO₂ (0.41) reported in the literature [25]. The higher intensity ratio, I(v'/v), with lower area percentage of u'' for the CeAl_{SS} support demonstrated that the Ce³⁺ state was the main component in the electronic Ce configuration followed by CeAl_{IS} and CeAl_{IC}. By using the following equation [44], the concentration of Ce³⁺ on the surface of the CeO₂-Al₂O₃ supports can be evaluated and the results are shown in Table 5.

$$\%Ce^{3+} = \frac{I_{v_0} + I_{v'} + I_{u_0} + I_{u'}}{\sum (I_{Ce^{3+}} + I_{Ce^{4+}})} \times 100 \quad (7)$$

The Ce³⁺ concentration on the surface of the CeAl_{SS} was the highest while those of CeAl_{IS} and CeAl_{IC} supports were similar, confirming that the Ce³⁺ ion state was a predominant species on the CeAl_{SS} surface. The surface atomic ratio, Ce/Al, obtained from the intensity of the elemental peak normalized by the relative sensitivity factor, is also given in Table 5. The lowest Ce/Al ratio was observed in the CeAl_{SS} support, followed by CeAl_{IC} and CeAl_{IS}, respectively. This evidently confirms the greater incorporation of the Ce species into the Al₂O₃ structure forming CeAlO₃ perovskite species during the condensation and gelation process in the single pot sol-gel preparation method than the impregnation methods. In addition, it was confirmed that larger Ce entity had been exposed on the surface of the promoted support prepared by the impregnation method, especially CeAl_{IS} support. This could be attributed to the nature of the impregnation method that allows the simultaneous adsorption and deposition of ceria precursors on the Al₂O₃ surface. The Ce/Al ratio of CeAl_{IS} being higher than that of CeAl_{IC} could have been due to the pore characteristic of the Al₂O₃ support. The slit-like plate with a wide pore mouth of Al₂O₃ provided paths for transporting and depositing ceria precursors inside the pores more easily than did the ink-bottle pore structure of Al₂O₃.

Additionally, it was found that the binding energies of O 1s for the supports derived solely by sol-gel and impregnated on sol-gel derived alumina, CeAl_{SS} and CeAl_{IS}, are in between that of pure CeO₂ (529.5 eV) and pure Al₂O₃ (531.3 eV) while the CeAl_{IC} has the value at 531.6 eV which is close to that of pure Al₂O₃. It clearly reveals that the interaction between CeO₂ and Al₂O₃ is attributed to the Ce-O-Al interaction [25,38] forming CeAlO₃ perovskite structure which can be initiated on the mesoporous structure of xerogel support. These XPS results are in accordance with the above characterization results.

3.2. Catalytic activity in steam reforming of glycerol

The glycerol steam reforming is complex and comprises a variety of reaction pathways to produce several liquid and gaseous products. Since all the catalysts convert glycerol completely, with the known conversions of glycerol to gaseous and solid (coke-deposited) products, the conversion to liquid product can be calculated from the mass balance: {(C in liquid product) = (C in feed) – (C in gas product) – (C in solid product)}. As shown in Table 6, gas is the main product, followed by smaller amounts of liquid and

Table 5

Binding energies of Al 2p, O 1s, and Ce 3d levels, surface atomic ratios, percentages of Ce³⁺, and *Intra*-component peak intensity for CeO₂-Al₂O₃ supports.

Supports	Binding Energy (eV)				Ce/Al	Area u''' (%)	Ce ³⁺ (%)	I(v/v)
	Al 2p	O 1s	Ce 3d _{5/2}	Ce 3d _{3/2} (u''')				
CeAl_SS	72.9	530.9	881.9	916.3	0.0075	7.1	35.4	0.70
CeAl_IS	73.7	530.7	882.0	916.3	0.0283	11.0	16.5	0.49
CeAl_IC	74.6	531.6	882.0	916.4	0.0094	12.4	14.3	0.42

solid products, respectively. The glycerol conversion into gas products and the gas product yields as functions of time-on-stream of all the catalysts are illustrated in Fig. 10. In terms of glycerol conversion into the gas phase, the NiCeAl_SS and NiCeAl_IS exhibited high average values (during 2–20 h) of 88.5% and 84.9%, respectively, whilst the value was much lower for NiCeAl_IC (69.7%). More importantly, the conversions over both the NiCeAl_SS and NiCeAl_IS

catalysts were steadily high throughout the reaction period. On the other hand NiCeAl_IC showed a high average conversion of 82.9% up to 13 h before dropping rapidly to 38.0% towards the end of the reaction period. The rapid decrease of the conversion into the gas phase is an indication of a severe deactivation of NiCeAl_IC, which is discussed in the next section.

In considering the gas products, all the catalysts provided the same major types, which were H₂, CO and CO₂, with small contents of CH₄ as shown in Fig. 10 with their yields. The trends of H₂ yield for all the catalysts were similar to that of the glycerol conversion into the gas phase. The high average H₂ yields for NiCeAl_SS and NiCeAl_IS catalysts at 66.7% and 64.4%, respectively, were obtained whereas the NiCeAl_IC catalyst provided a lower value at 44.4%. The average H₂ yields in terms of the moles of H₂ per mole of glycerol during 20 h of the reaction were 4.7, 4.5 and 3.1 for the NiCeAl_SS, NiCeAl_IS, and NiCeAl_IC catalysts, respectively. The values for the catalysts supported on the sol-gel derived support were much closer to the theoretical value (~6 mol H₂ per 1 mol of glycerol) [58–62] and even more on the traditional alumina.

For the CO₂ and CO yields, the average CO₂ yield was greater than the average CO yield for both NiCeAl_SS (45.6% vs. 38.9%) and NiCeAl_IS (45.0% vs 36.8%), but the yields were about the same for NiCeAl_IC. The greater CO₂ yield resulted from the water-gas-shift reaction, which is strongly promoted by CeO₂ [31,41,63,64]. The CeO₂ particles of NiCeAl_SS and NiCeAl_IS were more dispersed than that of NiCeAl_IC, thereby better enhancing the water-gas-shift reaction. In addition, CO was oxidized by the surface oxygen vacancies of CeO₂ [31].

Contrary to the H₂, CO, and CO₂ yields, the average CH₄ yields were about 4% and 3% over NiCeAl_SS and NiCeAl_IS, respectively, and were significantly less than that on the catalyst supported on the traditional alumina, NiCeAl_IC (6%). In addition, traces of C₂H₆ and C₂H₄ were detected solely on the NiCeAl_IC catalyst. This could possibly be attributed to the high surface area and the well-developed mesoporosity of sol-gel derived supports, which give the high number of active sites of the NiCeAl_SS and NiCeAl_IS catalysts. The steam reforming as well as the gasification of the adsorbed hydrocarbons on the catalyst's surface were thereby enhanced [27]. The traces could also be due to the presence of CeO₂ and CeAlO₃. The CeAlO₃ species was oxidized to form the CeO₂ species by capturing with CO₂ and the active CeO₂ reacted with the hydrocarbon species adsorbed at the Ni-support boundary and restored to the CeAlO₃ species [65].

The average selectivities of the gas products as summarized in Table 6 showed trends similar to those of the yields. These results show that the catalysts supported on the sol-gel-derived ceria-alumina xerogel were more active and stable than was the catalyst supported on the commercial non-xerogel alumina. The higher catalytic activity of NiCeAl_SS and NiCeAl_IS catalysts than NiCeAl_IC catalyst principally results from the greater number and dispersion of active Ni species, and the reducibility of NiCeAl_SS and NiCeAl_IS catalysts than those of the NiCeAl_IC catalyst, as observed in the H₂-chemisorption, TPR, XAS, and XPS results, respectively.

The qualitative results of the liquid products provide important information for comprehending the reaction pathway. The liquid products found in the condensable phase can be categorized into three main groups: (i) compounds with 3 carbon atoms hydrox-

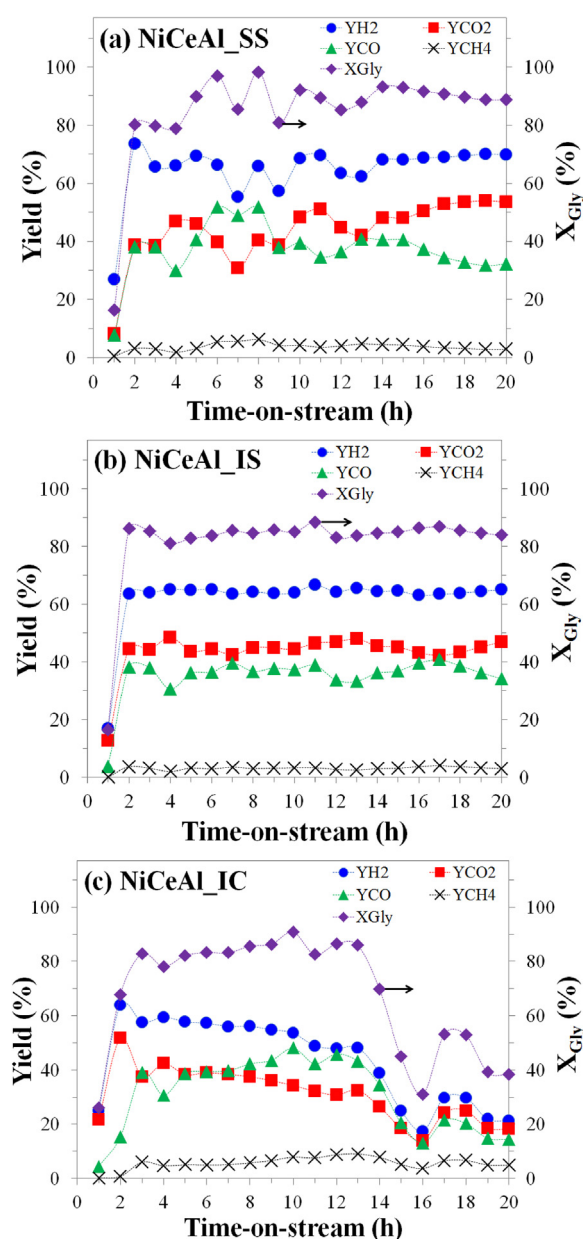


Fig. 10. Glycerol conversion into gas phase (Yield %) and gas products yield (H₂, CO₂, CO, CH₄) with time on stream of glycerol steam reforming at the molar ratio of water to glycerol of 9 at 700 °C over (a) NiCeAl_SS, (b) NiCeAl_IS and (c) NiCeAl_IC catalysts.

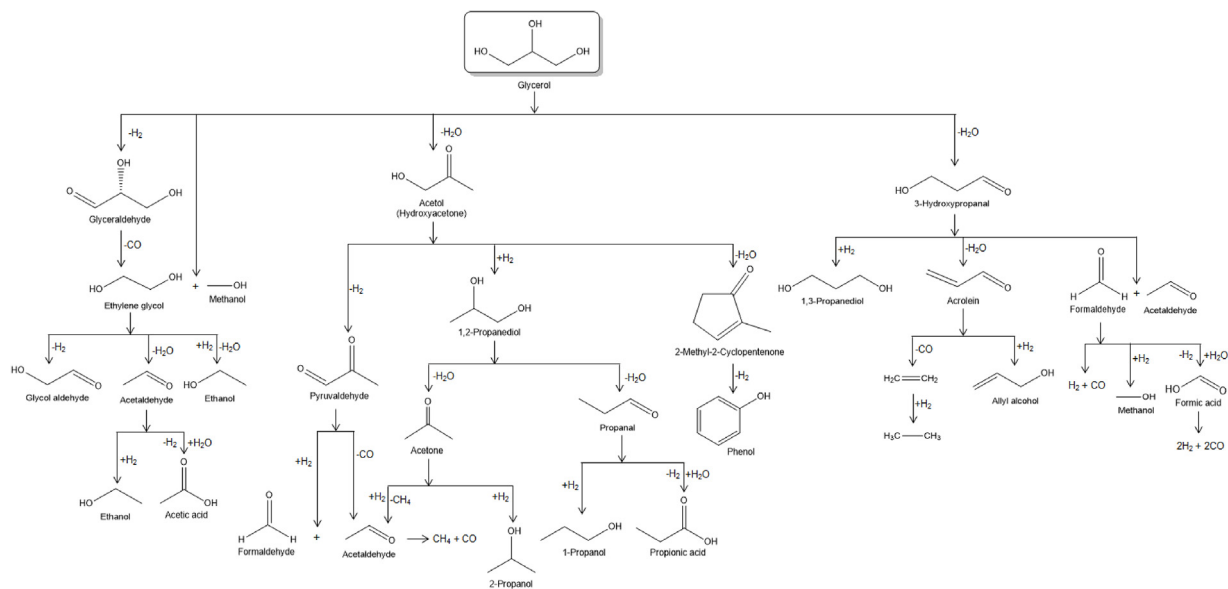


Fig. 11. Possible reaction pathways for glycerol conversion in steam reforming of glycerol.

yacetone (acetol), 1,2-propanediol, acetone, 1-propanol, propanal, allyl alcohol, and propionic acids), (ii) fewer than 3 carbon atoms (acetaldehyde, ethanol, acetic acid, methanol, and formic acid), and (iii) more than 3 carbon atoms (2 cyclopentenone and phenol). The common products detected for all the catalysts were acetaldehyde, acetone, methanol, ethanol, 1-propanol, propanal, allyl alcohol, and phenol. The products detected only for the two Ni catalysts supported on the $\text{CeO}_2\text{-Al}_2\text{O}_3$ oxides prepared by impregnation, NiCeAl_IC and NiCeAl_IS, were hydroxyacetone (acetol), 1,2-propanediol, formic acid, and acetic acid whereas propionic acid, ethylene glycol, and 2-cyclopentanone were detected only on NiCeAl_IC. Based on these products and referring to the published works [7,15,35,66–70], the reaction pathways of glycerol conversion in the steam reforming process can be outlined and shown in Fig. 11.

There are four main reaction routes of glycerol consisting of three types of reactions: dehydrogenation, hydrogenolysis, and dehydration. These reactions represent the effects of the bifunctional metal-acid properties of the catalysts [66]. The first and the second routes of glycerol dehydrogenation and hydrogenolysis generate a common product, such as ethylene glycol, which is converted to acetaldehyde, glycolaldehyde, and ethanol. The hydrogenolysis of glycerol also produces methanol. The third route is the glycerol dehydration to hydroxyacetone (acetol), which can be converted simultaneously in three ways to form a variety of products. The detected products verifying this pathway are 1,2 propanediol, acetone, propanal, 1-propanol, acetaldehyde, ethanol, formic acid, acetic acid, propionic acid, 2-cyclopentanone, and phenol. This pathway is caused by the activation of the terminal OH of glycerol on the Lewis acid sites, which is represented by the strong acid sites of the catalysts [71]. The fourth pathway is another glycerol dehydration reaction producing 3-hydroxypropanal, which is a starting reactant for the production of several chemicals. The species observed and confirming this pathway include allyl alcohol, acetaldehyde, methanol, formic acid, C_2H_4 , and C_2H_6 . This pathway involves the protonation of the secondary OH of glycerol to form acrolein, which favors the Brønsted acid sites mainly represented by the moderate acid sites that were classified [71]. The increase of the acid sites in NiCeAl_SS was mostly contributed by the increase of the CeAlO_3 phase. It has been reported that dehydration and dehydrogenation favor the acidity of support surfaces [66–68] such as alumina and CeAlO_3 .

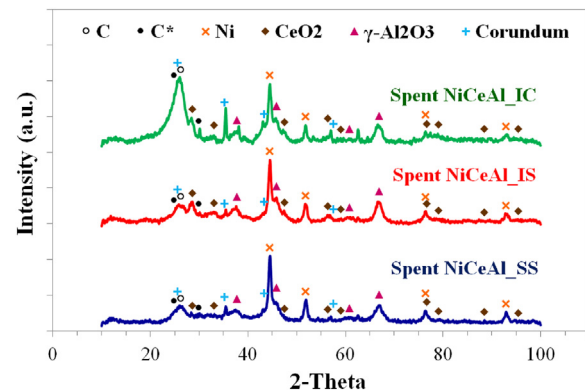


Fig. 12. XRD patterns of the spent NiCeAl_SS, NiCeAl_IS and NiCeAl_IC catalysts after 20-h glycerol steam reforming reaction.

All the acids (formic, acetic, and propionic), which were the condensable products obtained near the end of the pathways, were not detected on NiCeAl_SS whilst only propionic acid was not detected on NiCeAl_IS. These products could be catalytically reformed or hydrogenolyzed to smaller molecules such as H_2 , CO , and CO_2 on the active nickel sites [72–74]. With the higher number of active sites and Brønsted acid sites, NiCeAl_SS and NiCeAl_IS promoted the hydrogenolysis and dehydration/dehydrogenation of the acids to gaseous products, H_2 , CO , CH_4 and CO_2 [66,68], respectively, better than did NiCeAl_IC.

It was clearly shown that among the three catalysts, the Ni catalyst supported on $\text{CeO}_2\text{-Al}_2\text{O}_3$ prepared by the single-step sol-gel method was the most active one for glycerol steam reforming for producing hydrogen gas.

3.3. Characterization of spent catalysts

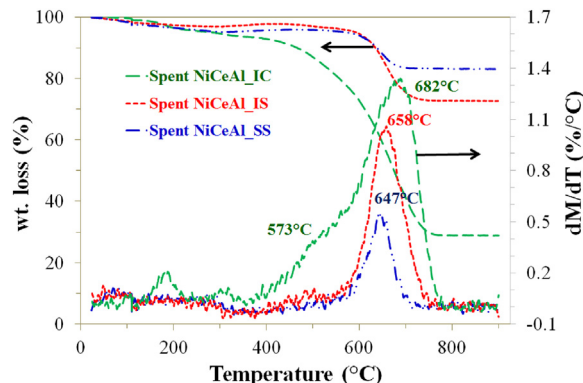
3.3.1. Crystalline structure of the catalysts

The XRD patterns of the spent NiCeAl_SS, NiCeAl_IS and NiCeAl_IC catalysts after performing the glycerol steam reforming are illustrated in Fig. 12. In addition to the phases found in the freshly reduced catalysts, the characteristic peaks of the carbon species and corundum or $\alpha\text{-Al}_2\text{O}_3$ were obtained. The peaks appearing at 26.3° (JCPDS 75-0444), and at 24.9° and 30.0° (JCPDS

Table 6

Selectivity of gas product, conversion to products, liquid products, and coke formation rate of the catalysts from glycerol steam reforming.

Catalysts	Selectivity of Gas Product (%)					%Conversion to products			Coke Yield ^c mmolC g _{cat} ⁻¹ h ⁻¹	Liquid Products
	H ₂	CO ₂	CO	CH ₄	C ₂ ^a	Gas	Liquid ^b	Solid		
NiCeAl_SS	80.0	51.5	44.1	4.4	0.0	88.5	10.9	0.6	0.6	Acetone, Acetaldehyde, Propanal, Methanol, Ethanol, 1-Propanol, Allyl alcohol, Phenol
NiCeAl_IS	77.2	54.2	42.3	3.5	0.0	84.9	14.1	1.0	1.4	Acetone, Acetaldehyde, Propanal, Methanol, Ethanol, 1-Propanol, Allyl alcohol, Acetol, 1,2-Propanediol, Formic acid, Acetic acid, Phenol
NiCeAl_IC	64.5	47.2	43.2	8.6	0.5	69.7	26.2	4.1	9.6	Acetone, Acetaldehyde, Propanal, Methanol, Ethanol, 1-Propanol, Allyl alcohol, Acetol, 1,2-Propanediol, Formic acid, Acetic acid, Propionic acid, Ethylene glycol, Phenol, 2 cyclopentanone

^a C₂H₄ and C₂H₆.^b Calculated from carbon balance.^c mmolC g_{cat}⁻¹ h⁻¹.**Fig. 13.** TGA and their derivative spectra of spent catalysts from glycerol steam reforming tested at 700 °C for 20-h reaction over the NiCeAl_SS, NiCeAl_IS and NiCeAl_IC catalysts.

74–2329) correspond to the two carbon species that had formed on the catalysts. It was clearly observed that the spent NiCeAl_IC catalyst had relatively greater intensities of the characteristic carbon peaks than did those of the spent NiCeAl_SS and NiCeAl_IS catalysts. Corundum or α -Al₂O₃, a more stable alumina phase, reflecting at 2-theta of 25.6°, 35.2°, 43.4°, and 57.5° was formed from the dehydration, followed by the sintering reaction of γ -Al₂O₃ [75–78]. Similar to the results of the catalyst deactivation by carbon deposition, the phase transformations of alumina in NiCeAl_SS and NiCeAl_IS were much less than that in NiCeAl_IC, as seen from the relatively lower intensities of the peaks corresponding to corundum in Fig. 12. Furthermore, after performing the reforming reaction, the crystallite size of Ni on NiCeAl_IC increased more than twice that of the freshly reduced catalyst (6.9 nm vs. 14.7 nm) whereas it increased about one-third for both the spent NiCeAl_SS and NiCeAl_IS catalysts, as shown by the values in Table 2. The increase of Ni particle size is due to sintering during the reaction causing the deactivation of the catalysts especially NiCeAl_IC [31,79,80]. Apart from the carbon formation and the transformation of γ -Al₂O₃, decreases in the CeO₂ characteristic peaks compared to all the freshly reduced catalysts, especially the NiCeAl_SS, were observed. This was attributed to the transformation of CeO₂ to the CeO_x and CeAlO₃ phases, although no diffraction peaks of those phases had been found, owing to the highly-dispersed phases of CeO_x and CeAlO₃. It was confirmed that the CeAlO₃ species had formed during the reaction.

3.3.2. Coke formation

The types of carbon species that had formed on the spent NiCeAl_SS, NiCeAl_IS and NiCeAl_IC catalysts were investigated using a thermogravimetric analyzer (TGA). Their TGA profiles and derivatives are shown in Fig. 13. Three main losses were observed in all of the spent catalysts with different extents and tempera-

tures. The initial loss below 200 °C is related to the removal of moisture and CO₂ adsorbed when the catalysts were kept under air at atmospheric pressure followed by the loss of the easily oxidized carbonaceous species [81,82]. The thermal decomposition of physisorbed carbonaceous products, termed as soft-coke, onto the catalyst surface occurs at the second step of the weight reduction between the temperatures of 200 °C and 400 °C. When the temperature was continuously elevated from 400 °C to 750 °C, a major decrease in the sample weight indicated the gasification of the bulky carbonaceous species or hard coke, generating CO and CO₂ (CO_x) [31,83,84]. The hard coke species in the range of 500–600 °C is associated with filamentous coke whilst it is graphitic carbon species for the higher temperature range of 600–700 °C. The spent NiCeAl_SS and NiCeAl_IS catalysts exhibited graphitic coke species at similar maximum temperatures of 647 °C and 658 °C, respectively, whereas both the filamentous and graphitic coke species appeared at 573 °C and 682 °C, respectively, for the spent NiCeAl_IC catalyst. This graphitic carbon is an inert coke that scarcely reacts with oxygen or steam [85].

From the area under the peak derivatives displayed in Fig. 13, the deactivation rate in terms of coke yield in the solid product was obtained and shown in Table 6. The table shows that NiCeAl_IC had been severely deactivated by coke formation at a coke yield of 9.6 mmolC g_{cat}⁻¹ h⁻¹ whilst the deactivation was much less pronounced on NiCeAl_SS and NiCeAl_IS (0.6 and 1.4 mmolC g_{cat}⁻¹ h⁻¹, respectively). In other words, the amount of graphitic carbon over the spent NiCeAl_IC catalyst was greater and more difficult to oxidize than those over the NiCeAl_SS and NiCeAl_IS catalysts because the steam reforming of glycerol over the NiCeAl_IC catalyst had produced larger amounts of CO, CH₄, and C₂ species than had the other catalysts. These gases were the initiating species of the coke deposited as some of them underwent a further Boudouard reaction, methane decomposition, and polymerization, respectively [31,83], forming different coke species on the catalyst surface. As previously mentioned, with the redox property of CeO₂, some of the CO and carbon species that had formed could have been oxidized by the surface oxygen atoms of CeO₂. However with the higher content of dispersed CeAlO₃ in NiCeAl_SS, these carbon species were close to complete oxidization, thereby giving markedly low coke yields. A similar result of coke deactivation on the Ni/CeO₂-Al₂O₃ prepared by the same impregnation method can be found in the work of Profeti et al. [12].

Comparing the results to those of the previous work [10,12,13] on glycerol steam reforming over Ni/CeO₂-Al₂O₃ catalysts prepared using different methods at similar operating condition as shown in Table 7, the catalyst prepared by the single-step sol-gel method in this work displayed remarkable activity and stability by giving the highest H₂ yield of 80% and the lowest coke formation (5–28 times lower).

Table 7Comparison of glycerol steam reforming results over Ni/CeO₂/Al₂O₃ with previous studies.

Catalysts	Condition				H ₂ Selectivity (%)	Coke formation (%)	Source
	S:G ^a	T (°C)	GHSV (h ⁻¹)	Time (h)			
Ni/CeO ₂ -Al ₂ O ₃	9	700	42,000	20	80	0.6	This study
Ni/CeO ₂ /Al ₂ O ₃	6	700	51,000	1	58	N/A	[10]
Ni/CeO ₂ /γ-Al ₂ O ₃	6	700	N/A	6	62	3.2	[12]
Ni/CeO ₂ /α-Al ₂ O ₃	6	600	39,000	10	N/A	17	[13]

^a S:G = Molar ratio of steam to glycerol.

4. Conclusions

In this work, three CeO₂-Al₂O₃ oxides were prepared by a single-step sol-gel method and impregnation of cerium precursors on two types of Al₂O₃, of which one was a commercial alumina whilst the other was a prepared xerogel. These oxides were investigated for their physical and chemical properties, as well as their effects on the catalytic behaviors of the Ni catalysts supported on these oxides towards glycerol steam reforming reaction. The different pore structures of CeO₂-Al₂O₃ were strongly affected by the original textural properties of the Al₂O₃ supports. The high surface area supports with narrow pore size distributions and mesoporous structures were achieved when the promoted supports, CeAl_{1.5}SS and CeAl_{1.5}S, were derived based on sol-gel method. The mesoporous support generated by the sol-gel method enhances the incorporation of the Ce species into the Al₂O₃ structure to form a CeAlO₃ perovskite structure more than does the traditional method. The formation of this species suppresses any strong interaction between the nickel species and the Al₂O₃ support, thereby increasing the number of active sites and the reducibility of the active nickel species. Another important contribution of the CeAlO₃ phase to the oxide is to increase in Brønsted acid sites. Hence, the Ni active sites combined with the Brønsted acid sites promote the hydrogenolysis and dehydrogenation-dehydration of the bifunctional metal-acid Ni/CeO₂-Al₂O₃ catalyst, thereby converting more condensable intermediates into gaseous products, as well as leading to higher glycerol conversion and H₂ yield in glycerol steam reforming. In addition, CeAlO₃ strongly inhibits coke formation, Ni sintering, and the transformation of the alumina phase, thereby producing excellent stability in the catalyst. Consequently, the single-step sol-gel method is a promising method for preparing CeO₂-Al₂O₃ support of a Ni catalyst utilized in glycerol steam reforming for hydrogen production.

Acknowledgements

The authors would like to express their appreciation to the Joint Graduate School of Energy and Environment (JGSEE), King Mongkut's University of Technology Thonburi (KMUTT) through the "KMUTT 55th Anniversary Commemorative Fund", and the Higher Education Research Promotion and National Research University (NRU) Project of Thailand, Office of the Higher Education Commission for the financial support of this research. Our appreciation also goes to the Synchrotron Light Research Institute (SLRI) for a beam time XAS.

References

- [1] A. Iriondo, V.L. Barrio, J.F. Cambra, P.L. Arias, M.B. Güemez, R.M. Navarro, M.C. Sánchez-Sánchez, J.L.G. Fierro, *Top. Catal.* 49 (2008) 46–58.
- [2] M.E. Sad, H.A. Duarte, Ch. Vignatti, C.L. Padró, C.R. Pesteguía, *Int. J. Hydrogen Energy* 40 (2015) 6097–6106.
- [3] C.A. Franchini, W. Aranzaez, A.M. Duarte de Fraias, G. Pecchi, M.A. Fraga, *Appl. Catal. B: Environ.* 147 (2014) 193–202.
- [4] M. Slinn, K. Kendall, C. Mallon, J. Andrews, *Bioresour. Technol.* 99 (2008) 5851–5858.
- [5] A. Ebshish, Z. Yaakob, Y.H. Taufiq-Yap, A. Bshish, A. Shaibani, *J. Fuel Cell Sci. Technol.* 10 (2013), 021003:1–021003:6.
- [6] B. Zhang, X. Tang, Y. Li, Y. Xu, W. Shen, *Int. J. Hydrogen Energy* 32 (2007) 2367–2373.
- [7] V. Chioldo, S. Freni, A. Galvagno, N. Mondello, F. Frusteri, *Appl. Catal. A: Gen.* 381 (2010) 1–7.
- [8] T. Hirai, N. Ikenaga, T. Miyake, T. Suzuki, *Energy Fuels* 19 (2005) 1761–1762.
- [9] R. Sundar, P.D. Vaidya, *Energy Fuels* 26 (2012) 4195–4204.
- [10] S. Adhikari, S. Fernando, A. Haryanto, *Catal. Today* 129 (2007) 355–364.
- [11] M. El Doukkali, A. Iriondo, P.L. Arias, J.F. Cambra, I. Gandarias, V.L. Barrio, *Int. J. Hydrogen Energy* 37 (2012) 8298–8309.
- [12] L.P.R. Profeti, E.A. Ticianelli, E.M. Assaf, *Int. J. Hydrogen Energy* 34 (2009) 5049–5060.
- [13] I.N. Buffoni, F. Pompeo, G.F. Santori, N.N. Nichio, *Catal. Commun.* 10 (2009) 1656–1660.
- [14] Y. Choi, N.D. Kim, J. Baek, W. Kim, H.J. Lee, J. Yi, *Int. J. Hydrogen Energy* 36 (2011) 3844–3852.
- [15] A. Iriondo, V.L. Barrio, J.F. Cambra, P.L. Arias, M.B. Guemez, M.C. Sanchez-Sánchez, R.M. Navarro, J.L.G. Fierro, *Int. J. Hydrogen Energy* 35 (2010) 11622–11633.
- [16] E.A. Sánchez, M.A. D'Angelo, R.A. Comelli, *Int. J. Hydrogen Energy* 35 (2010) 5902–5907.
- [17] C.D. Dave, K.K. Pant, *Renew. Energy* 36 (2011) 3195–3202.
- [18] S. Adhikari, S.D. Fernando, S.D. Filip To, R. Mark Bricka, P.H. Steele, A. Haryanto, *Energy Fuels* 22 (2008) 1220–1226.
- [19] L. Rossetti, A. Gallo, V.D. Santo, C.L. Bianchi, V. Nichele, M. Signoretto, E. Finocchio, G. Ramis, A.D. Michele, *ChemCatChem* 5 (2013) 294–306.
- [20] E.A. Sanchez, R.A. Comelli, *Int. J. Hydrogen Energy* 37 (2012) 14740–14746.
- [21] P. Osorio-Vargas, N.A. Flores-González, R.M. Navarro, J.L.G. Fierro, C.H. Campos, P. Reyes, *Catal. Today* 259 (2015) 27–38.
- [22] A. Rakib, C. Gennequin, T. Dhaïnaut, S. Ringot, A. Aboukaïs, E. Abi-Aad, *Adv. Mater. Res.* 324 (2011) 153–156.
- [23] C. Xie, Y. Chen, Y. Li, X. Wang, C. Song, *Appl. Catal. A: Gen.* 390 (2010) 210–218.
- [24] A. Iriondo, V.L. Barrio, M. El Doukkali, J.F. Cambra, M.B. Güemez, J. Requieres, P.L. Arias, M.C. Sánchez-Sánchez, R. Navarro, J.L.G. Fierro, *Int. J. Hydrogen Energy* 37 (2012) 2028–2036.
- [25] A.P. Ferreira, D. Zanchet, R. Rinaldi, U. Schuchardt, S. Damyanova, J.M.C. Bueno, *Appl. Catal. A: Gen.* 388 (2010) 45–56.
- [26] L. Ji, J. Lin, K.L. Tan, H.C. Zeng, *Chem. Mater.* 12 (2000) 931–939.
- [27] J.G. Seo, M.H. Youn, K.M. Cho, S. Park, I.K. Song, *J. Power Sources* 173 (2007) 943–949.
- [28] A. Vázquez, T. López, R. Gómez, X. Bokhimi, A. Morales, O. Novaro, *J. Solid State Chem.* 128 (1997) 161–168.
- [29] A. Vázquez, T. Lopez, R. Gomez, X. Bokhimi, *J. Mol. Catal. A: Chem.* 167 (2001) 91–99.
- [30] R. Guo, Y. Zhou, W. Pan, J. Hong, W. Zhen, Q. Jin, C. Ding, S. Guo, *J. Ind. Eng. Chem.* 19 (2013) 2022–2025.
- [31] N. Srisirwat, S. Therdthianwong, A. Therdthianwong, *Int. J. Hydrogen Energy* 34 (2009) 2224–2234.
- [32] K. Kamonsuengkasem, S. Therdthianwong, A. Therdthianwong, *Fuel Process. Technol.* 106 (2013) 695–703.
- [33] P. Kim, Y. Kim, H. Kim, I.K. Song, J. Yi, *Appl. Catal. A: Gen.* 272 (2004) 157–166.
- [34] A.C. Pierre, *Introduction to Sol-Gel Processing*, Kluwer Academic Publishers, Boston, 1998.
- [35] G. Wu, C. Zhang, S. Li, Z. Han, T. Wang, X. Ma, J. Gong, *ACS Sustain. Chem. Eng.* 1 (2013) 1015–1062.
- [36] F. Ocampo, B. Louis, L. Kiwi-Minsker, A. Roger, *Applied Catal. A: Gen.* 392 (2011) 36–44.
- [37] J.Z. Shyu, W.H. Weber, H.S. Gandhi, *J. Phys. Chem.* 92 (1988) 4964–4970.
- [38] S. Damyanova, C.A. Perez, M. Schmai, J.M.C. Bueno, *Appl. Catal. A: Gen.* 234 (2002) 271–282.
- [39] R. Ramírez-López, L. Balderas-Tapia, I. Elizalde-Martínez, T. Viveros, *Chem. Eng. Commun.* 196 (2009) 1189–1197.
- [40] S. Shao, A.W. Shi, C.L. Liu, R.Z. Yang, W.S. Dong, *Fuel Process. Technol.* 125 (2014) 1–7.
- [41] L. Ilieva, G. Pantaleo, I. Ivanov, A.M. Venezia, D. Andreeva, *Appl. Catal. B: Environ.* 65 (2006) 101–109.
- [42] A.C.S.F. Santos, S. Damyanova, G.N.R. Teixeira, L.V. Mattos, F.B. Noronha, F.B. Passos, J.M.C. Bueno, *Appl. Catal. A: Gen.* 290 (2005) 123–132.
- [43] Panagiotopoulou (2006).

[44] M. El Doukkali, A. Iriondo, P.L. Arias, J. Requier, I. Gandarías, L. Jalowiecki-Duhamel, F. Dumeignil, *Appl. Catal. B: Environ.* 125 (2012) 516–529.

[45] Y. Shen, S. Zhu, T. Qiu, S. Shen, *Catal. Commun.* 11 (2009) 20–23.

[46] V.R. Choudhary, V.H. Rane, *J. Catal.* 130 (1991) 411–422.

[47] S. Sato, R. Takahashi, M. Kobune, H. Gotoh, *Appl. Catal. A: Gen.* 356 (2009) 57–63.

[48] J. Lif, I. Odenbrand, M. Skoglundh, *Appl. Catal. A: Gen.* 317 (2007) 62–69.

[49] M. Meng, P. Lin, Y. Fu, *Spectrosc. Lett.* 34 (2001) 83–92.

[50] J. El Fallah, S. Boujana, H. Dexpert, A. Kienemann, J. Majerus, O. Touret, F. Villain, F. Le Normand, *J. Phys. Chem.* 98 (1994) 5522–5533.

[51] S. Chowdhury, K.S. Lin, *Mater. Chem. Phys.* 133 (2012) 163–169.

[52] Y. Takahashi, H. Sakami, M. Nomura, *Anal. Chim. Acta* 468 (2002) 345–354.

[53] A. Martínez-Arias, M. Fernández-García, L.N. Salamanca, R.X. Valenzuela, J.C. Conesa, J. Soria, *J. Phys. Chem. B* 104 (2000) 4038–4046.

[54] T.R. Reina, W. Xu, S. Ivanova, M.A. Centeno, J. Hanson, J.A. Rodriguez, J.A. Odriozola, *Catal. Today* 205 (2013) 41–48.

[55] NIST X-ray photoelectron spectroscopy database, Version 4.1 (National Institute of Standards and Technology, Gaithersburg, 2012). Available online: <http://srdata.nist.gov/xps/>.

[56] C. Yu, J. Hu, W. Zhou, Q. Fan, *J. Energy Chem.* 23 (2014) 235–243.

[57] M.V. Rama Rao, T. Shripathi, *J. Electron Spectrosc. Relat. Phenom.* 87 (1997) 121–126.

[58] X. Wang, S. Li, H. Wang, B. Liu, X. Ma, *Energy Fuels* 22 (2008) 4285–4291.

[59] S. Adhikari, S. Fernando, A. Haryanto, *Energy Fuels* 21 (2007) 2306–2310.

[60] S. Adhikari, S. Fernando, S.R. Gwaltney, S.D. Fillip To, R.M. Bricka, P.H. Steele, A. Haryanto, *Int. J. Hydrogen Energy* 32 (2007) 2875–2880.

[61] A. Lima da Silva, I.L. Müller, *Int. J. Hydrogen Energy* 36 (2011) 2057–2075.

[62] C. Wang, B. Dou, H. Chen, Y. Shen, Y. Xu, X. Du, T. Luo, C. Tan, *Chem. Eng. J.* 220 (2013) 133–142.

[63] J. Nishikawa, K. Nakamura, M. Asadullah, T. Miyazawa, K. Kunimori, K. Tomishige, *Catal. Today* 131 (2008) 146–155.

[64] L.F. Bobadilla, A. Penkova, A. Álvarez, M.I. Domínguez, F. Romero-Sarria, M.A. Centeno, J.A. Odriozola, *Appl. Catal. A: Gen.* 492 (2015) 38–47.

[65] W. Chen, G. Zhao, Q. Xue, L. Chen, Y. Lu, *Appl. Catal. B: Environ.* 136–137 (2013) 260–268.

[66] B.C. Miranda, R.J. Chimentão, J.B.O. Santos, F. Gispert-Guirado, J. Lliorca, F. Medina, F. López Bonillo, J.E. Sueiras, *Appl. Catal. B: Environ.* 147 (2014) 464–480.

[67] L.F. Bobadilla, A. Penkova, F. Romero-Sarria, M.A. Centeno, J.A. Odriozola, *Int. J. Hydrogen Energy* 39 (2014) 5704–5712.

[68] K.N. Papageridis, G. Siakavelas, N.D. Charisiou, D.G. Avraam, L. Tzounis, K. Kousi, M.A. Goula, *Fuel Process. Technol.* 152 (2016) 156–175.

[69] F. Pompeo, G. Santori, N.N. Nichio, *Int. J. Hydrogen Energy* 35 (2010) 8912–8920.

[70] Y.C. Lin, *Int. J. Hydrogen Energy* 38 (2013) 2678–2700.

[71] D. Stošić, S. Bennici, S. Sirotin, C. Calais, J.-L. Couturier, J.-L. Doubois, A. Travert, A. Auroux, *Appl. Catal. A: Gen.* 447–448 (2012) 124–134.

[72] A.C. Basagiannis, X.E. Verykios, *Int. J. Hydrogen Energy* 32 (2007) 3343–3355.

[73] K.K. Pant, P. Mohanty, S. Agarwal, A.K. Dalai, *Catal. Today* 207 (2013) 36–43.

[74] X. Yang, Y. Wang, M. Li, B. Sun, Y. Li, Y. Wang, *Energy Fuels* 30 (2016) 2198–2203.

[75] J.G. Seo, M.H. Youn, S. Park, I.K. Song, *Int. J. Hydrogen Energy* 33 (2008) 7427–7434.

[76] C. Kaya, F. Kaya, A.R. Boccaccini, K.K. Chawla, *Acta Mater.* 49 (2001) 1189–1197.

[77] S. Therdthianwong, N. Srisirivat, A. Therdthainwong, E. Croiset, *Int. J. Hydrogen Energy* 36 (2011) 2877–2886.

[78] L.A. O'Dell, S.L.P. Savin, A.V. Chadwick, M.E. Smith, *Solid State Nucl. Magn. Reson.* 31 (2007) 169–173.

[79] H. Chen, H. Yu, F. Penga, G. Yanga, *Chem. Eng. J.* 160 (2010) 333–339.

[80] V. Palma, C. Ruocco, *Int. J. Hydrogen Energy* 42 (2017) 1598–1608.

[81] E.V. Vasiliadou, A.A. Lemonidou, *Appl. Catal. A: Gen.* 396 (2011) 117–185.

[82] A.I. Tsyganok, T. Tsunoda, S. Hamakawa, K. Suzuki, K. Takehira, T. Hayakawa, *J. Catal.* 213 (2003) 191–203.

[83] H. Zhang, S. Shao, R. Xiao, D. Shen, J. Zeng, *Energy Fuels* 28 (2014) 52–57.

[84] S.K. Sahoo, S.S. Ray, I.D. Singh, *Appl. Catal. A: Gen.* 278 (2004) 83–91.

[85] K.Y. Koo, S. Lee, U.H. Jung, H. Roh, W.L. Yoon, *Fuel Process. Technol.* 119 (2014) 151–157.